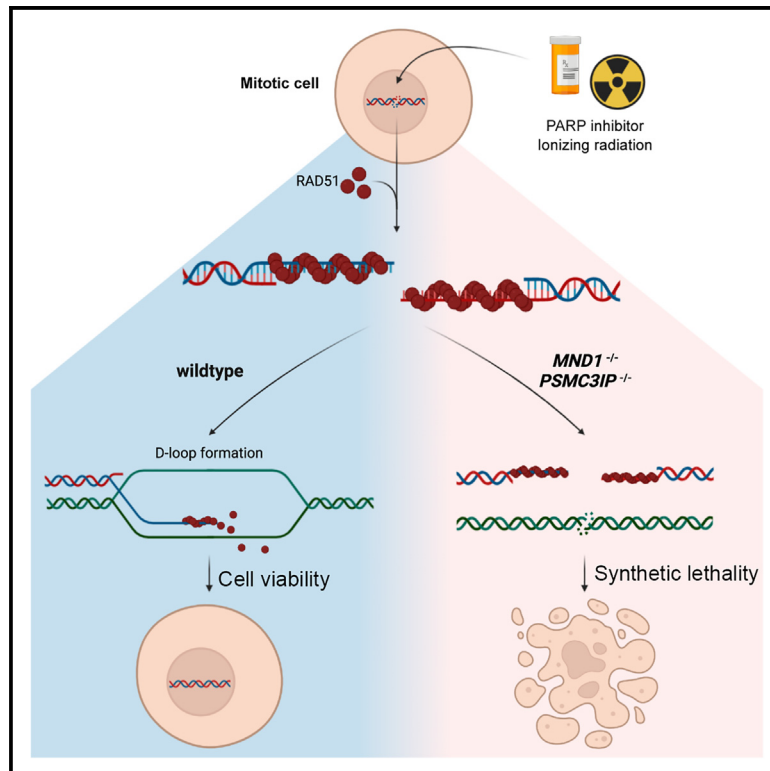


MND1 and PSMC3IP control PARP inhibitor sensitivity in mitotic cells

Graphical abstract



Authors

Anabel Zelceski, Paola Francica, Lea Lingg, ..., Andrew N.J. Tutt, Sven Rottenberg, Christopher J. Lord

Correspondence

Stephen.pettitt@icr.ac.uk (S.J.P.), Andrew.tutt@icr.ac.uk (A.N.J.T.), sven.rottenberg@vetsuisse.unibe.ch (S.R.), Chris.lord@icr.ac.uk (C.J.L.)

In brief

Processes used by meiotic cells to recombine chromosomes are also often co-opted in mitotic DNA repair. Zelceski et al. show that the meiotic PSMC3IP-MND1 heterodimer plays a critical role in the response to DNA damage in mitotic cells, including the response to PARPi used in cancer treatment.

Highlights

- The PSMC3IP-MND1 heterodimer controls meiotic DNA recombination
- PSMC3IP-MND1 controls mitotic recombination
- PSMC3IP-MND1 loss causes PARPi sensitivity genes in mitotic cells
- PSMC3IP-MND1 loss causes a D loop defect and toxic RAD51



Article

MND1 and PSMC3IP control PARP inhibitor sensitivity in mitotic cells

Anabel Zelceski,^{1,2,9} Paola Francica,^{3,4,9} Lea Lingg,^{3,4} Merve Mutlu,³ Colin Stok,⁵ Martin Liptay,³ John Alexander,² Joseph S. Baxter,^{1,2} Rachel Brough,^{1,2} Aditi Gulati,² Syed Haider,² Maya Raghunandan,² Feifei Song,^{1,2} Sandhya Sridhar,^{1,2} Josep V. Forment,⁶ Mark J. O'Connor,⁶ Barry R. Davies,⁶ Marcel A.T.M. van Vugt,⁶ Dragomir B. Krastev,^{1,2} Stephen J. Pettitt,^{1,2,*} Andrew N.J. Tutt,^{2,*} Sven Rottenberg,^{3,4,7,8,*} and Christopher J. Lord^{1,2,10,*}

¹The CRUK Gene Function Laboratory, The Institute of Cancer Research, London SW3 6JB, UK

²Breast Cancer Now Toby Robins Research Centre, The Institute of Cancer Research, London SW3 6JB, UK

³Institute of Animal Pathology, Vetsuisse Faculty, University of Bern, 3012 Bern, Switzerland

⁴Departement of Biomedical Research (DBMR), Cancer Therapy Resistance Cluster, University of Bern, 3012 Bern, Switzerland

⁵Department of Medical Oncology, University Medical Center Groningen, University of Groningen, Hanzeplein 1, 9713GZ Groningen, the Netherlands

⁶Oncology R&D, AstraZeneca, Cambridge, UK

⁷Division of Molecular Pathology, The Netherlands Cancer Institute, 1066CX Amsterdam, the Netherlands

⁸Bern Center for Precision Medicine, University of Bern, 3012 Bern, Switzerland

⁹These authors contributed equally

¹⁰Lead contact

*Correspondence: Stephen.pettitt@icr.ac.uk (S.J.P.), Andrew.tutt@icr.ac.uk (A.N.J.T.), sven.rottenberg@vetsuisse.unibe.ch (S.R.), Chris.lord@icr.ac.uk (C.J.L.)

<https://doi.org/10.1016/j.celrep.2023.112484>

SUMMARY

The PSMC3IP-MND1 heterodimer promotes meiotic D loop formation before DNA strand exchange. In genome-scale CRISPR-Cas9 mutagenesis and interference screens in mitotic cells, depletion of *PSMC3IP* or *MND1* causes sensitivity to poly (ADP-Ribose) polymerase inhibitors (PARPi) used in cancer treatment. *PSMC3IP* or *MND1* depletion also causes ionizing radiation sensitivity. These effects are independent of PSMC3IP/MND1's role in mitotic alternative lengthening of telomeres. *PSMC3IP*- or *MND1*-depleted cells accumulate toxic RAD51 foci in response to DNA damage, show impaired homology-directed DNA repair, and become PARPi sensitive, even in cells lacking both *BRCA1* and *TP53BP1*. Epistasis between *PSMC3IP-MND1* and *BRCA1/BRCA2* defects suggest that abrogated D loop formation is the cause of PARPi sensitivity. Wild-type *PSMC3IP* reverses PARPi sensitivity, whereas a *PSMC3IP* p.Glu201del mutant associated with D loop defects and ovarian dysgenesis does not. These observations suggest that meiotic proteins such as MND1 and PSMC3IP have a greater role in mitotic DNA repair.

INTRODUCTION

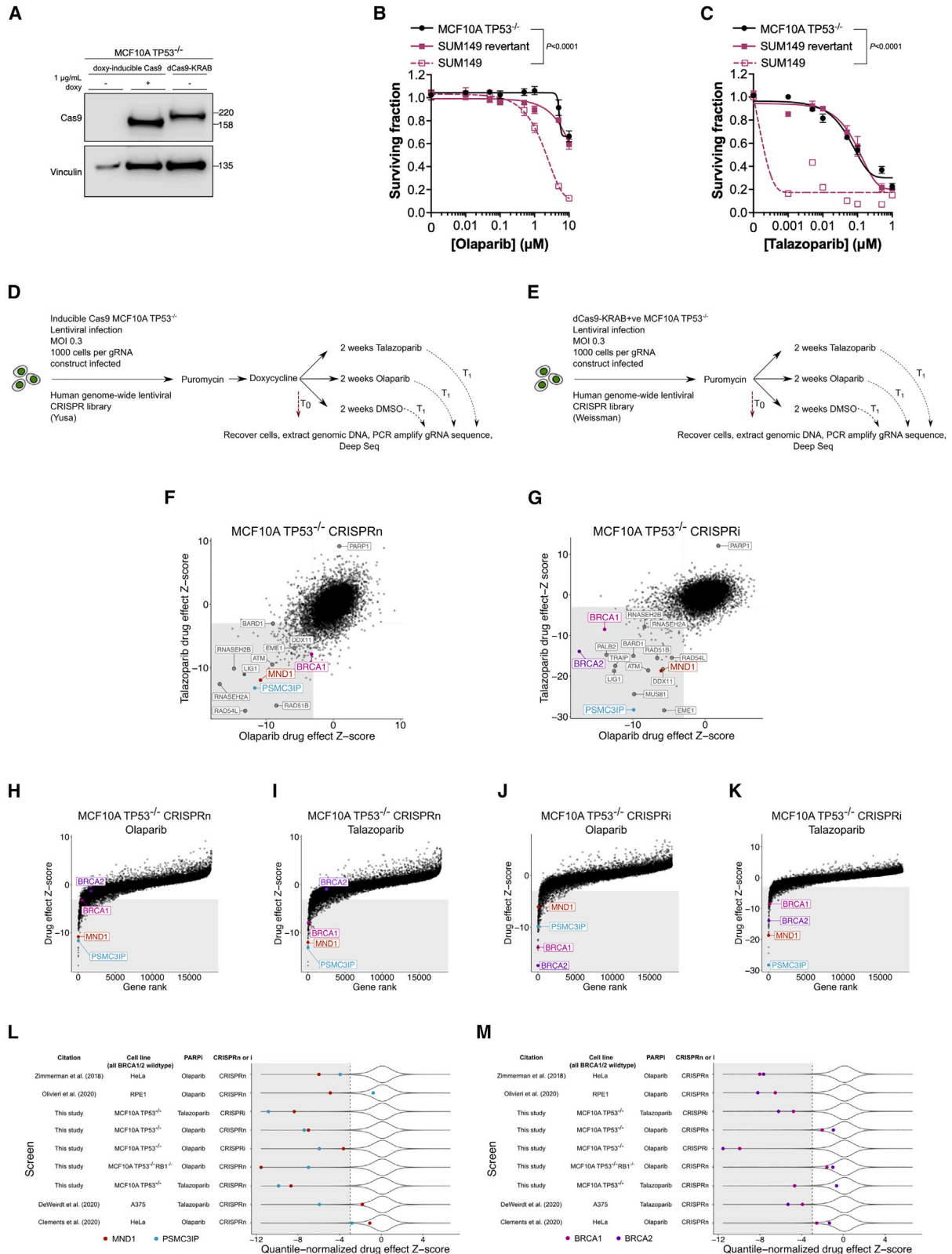
Five different poly(ADP-ribose) polymerase inhibitors (PARPi)^{1,2} are approved for the treatment of homologous recombination (HR)-defective cancer.^{3,4} PARPi work by generating a synthetic lethal⁵ DNA lesion, namely chromatin associated (trapped) poly(ADP-ribose) polymerase 1 (PARP1).⁶ The nucleoprotein complex caused by trapped PARP1 provides a steric barrier to the normal function of DNA and impairs normal replication fork (RF) function.⁷ The DNA damage caused by PARPi is repaired by BRCA1-, BRCA2-, and RAD51-mediated HR; in their absence, cytotoxicity ensues.² Trapped PARP1 at replication gaps between Okazaki fragments is also a major cause of PARPi sensitivity.^{8–10} Targeting PARP1 in patients with HR-defective cancers is a prime example of the concept of precision medicine in cancer therapy.¹¹

To identify patients with HR-defective tumors, various approaches are used, including the detection of *BRCA1/2* or

other HR-associated gene mutations,¹² prior platinum sensitivity,¹³ or a genomic mutational signature that reflects the lack of HR and predominance of other DNA repair pathways.^{14–17} Experimentally, PARPi sensitivity is predicted by the inability to localize the DNA recombinase RAD51 to the site of DNA damage.^{18–20}

To better understand what determines PARPi sensitivity, we carried out a series of parallel CRISPR mutagenesis and interference screens. Both mutagenesis and interference screens identified the meiotic recombination heterodimer MND1-PSMC3IP as controlling PARPi response in mitotic cells. In contrast with *BRCA1* or *BRCA2* mutant cells, *MND1*- or *PSMC3IP*-deficient mitotic cells accumulate RAD51 foci in response to DNA damage, a result of defective HR processing. These effects are reversed by ectopic expression of *MND1* or *PSMC3IP*, but not by a *PSMC3IP* mutant with an inability to form productive D loops, which are critical for effective HR.





(legend on next page)

RESULTS

Parallel CRISPR mutagenesis and interference screens identify *MND1* and *PSMC3IP* as highly penetrant determinants of PARPi sensitivity

We carried out parallel CRISPR mutagenesis (CRISPRn) and CRISPR interference (CRISPRi) chemosensitivity screens using a PARPi-resistant, HR-proficient, non-tumor epithelial cell line with an engineered *TP53* mutation, MCF10A *TP53*^{-/-}. We used *TP53* mutant MCF10A cells, as many cancer-associated mutations (such as *BRCA1*^{21–23}) impair cellular fitness by invoking *TP53*-mediated cell cycle checkpoints. We introduced into these cells either a doxycycline-inducible Cas9 transgene (Cas9) or a transgene expressing catalytically inactive Cas9 (dCas9) fused to the KRAB transcriptional repressor²⁴ (Figure 1A). We confirmed PARPi resistance in these cells, using *BRCA1* mutant SUM149 triple negative breast tumor cell lines with a PARPi-resistance causing *BRCA1* reversion mutation^{11,25} as a control (Figures 1B and 1C).

For the CRISPRn screen, we mutagenized Cas9⁺ cells with a genome-wide single guide RNA (sgRNA) library³⁰ (Figure 1D). After removing non-transduced cells and a fraction of the cell population for later analysis (T₀ sample), the resultant cell population was divided into three cohorts exposed to (1) the drug vehicle (DMSO); (2) olaparib; or (3) talazoparib. We used concentrations of PARPi sufficient to cause a 20% decrease in the cell population (surviving fraction 80 concentration) to maximize the potential for identifying sensitization effects. Cells were continuously cultured in the presence of drug (or DMSO) for 2 weeks, at which point DNA from surviving cells was recovered (T₁ sample). Using deep sequencing, we compared the relative enrichment or depletion of sgRNAs from T₀ vs. T₁ samples and used these data to calculate normalized drug effect Z-scores (normZ³¹) for each gene (Tables S1A–S1C). We used an assessment of the depletion of sgRNA targeting core essential genes as a quality control measure,³² an approach that indicated that each of the screens was of sufficient quality to warrant further analysis (Figures S1A–S1C, Tables S1B and S1C).

In parallel, we also conducted genome-wide CRISPRi screens³³ for olaparib or talazoparib sensitivity in dCas9-KRAB⁺ MCF10A *TP53*^{-/-} cells (Figure 1E). When we compared data from olaparib vs. talazoparib screens, we found both CRISPRi and CRISPRn screens to be highly reproducible (Figures 1F and 1G).

Deletion of *PARP1* or *PARP1* mutations that prevent PARP1 trapping cause PARPi resistance,⁷ both in *BRCA1* wild-type and *BRCA1* mutant cells.³⁴ *PARP1* sgRNA gave one of the most profound resistance-causing effects in both CRISPRn and CRISPRi screens (Figures 1F and 1G). Previous focused short hairpin RNA (shRNA) screens,³⁵ genome-wide shRNA screens (Table S1D),²⁵ and genome-wide CRISPR-Cas9 screens for PARPi sensitivity^{26–29,36} indicated that the genes involved in HR enhance PARPi sensitivity when inactivated. This was also the case in our CRISPRn and CRISPRi screens. Some of the most profound PARPi sensitivity-causing effects were caused by CRISPRi or CRISPRn targeting of the HR-associated genes *RAD51B*, *RAD54L*, *EME1*, *ATM*, *MUS81*, *PALB2*, *BRCA1*, *BARD1*, *BRCA2*, and *DDX11* (Figures 1F and 1G); unbiased pathway annotation of “hits” in CRISPRn and CRISPRi screens identified HR as an enriched pathway (KEGG “HR” p values of 5.5×10^{-10} , 1.1×10^{-8} , 9.4×10^{-16} , and 1.9×10^{-12} for olaparib/CRISPRn, talazoparib/CRISPRn, olaparib/CRISPRi, and talazoparib/CRISPRi screens, respectively (Tables S1E–S1H). In addition to the genes described above, additional genes involved in HR and double-strand break repair also scored as “hits” in our screen (*ACTR5*, *ATM*, *ATRIP*, *AUNIP*, *CHAF1B*, *FAAP24* [*C19orf40*], *FANCA*, *FANCD2*, *FANCE*, *FANCI*, *FANCL*, *FANCM*, *INO80*, *KIAA1524* [*CIP2A*], *MCM8*, *MCM9*, *MRE11A*, *NBN*, *NSMCE1*, *NDNL2*, *PNKP*, *RAD50*, *RAD51*, *RAD51C*, *RAD51AP1*, *RBBP8* [*CtIP*], *RMI1*, *RNF8*, *RNF168*, *SHFM1* [*DSS1*], *SLX4*, *SMC4*, *SMC6*, *SFR1*, *STRA13* [*CENPX*], *SLX4*, *SWI5*, *TELO*, *TONSL*, *TRAIIP*, *USP1*, *WDR48*, *WRN*, *XRCC2*, and *XRCC3*), as did genes implicated in recruitment and activity of the 9-1-1 complex (*ATAD5*, *RAD1*, *RAD9A*, and *RAD17*), those that control the DNA damage-induced S/G₂ and G₂/M checkpoints (*FOXM1*, *CCNB2*), chromatin remodeling complex component-coding genes (*ACTL6A*, *BRD2*, *RBBP7*, and *SMARCB1*), chromosome cohesion factors (*CHTF18*, *CHTF8*, *ESCO2*, and *DSCC1*), base excision repair genes (*LIG1*, *LIG3*, *FEN1*, *UNG*, *APEX2*, and *MUTYH*) and nucleotide excision repair genes (*CUL4A*, *GTF2H2C*, *RFC4*, *LIG1*, *RPA3*, *POLD2*, *ERCC2*, *GTF2H3*, *RFC5*, *PCNA*, *RFC1*, *CCNH*, *CETN2*, *GTF2H4*, *DDB1*, *POLE4*, *CDK7*, and *ERCC3*). In addition, the PARP1 co-factor *C4orf27* (*HPF1*) and three *RNA-SEH2* family genes known to control PARPi sensitivity by modulating levels of genomic uracil (*RNASEH2A*, *RNASEH2B*, and *RNASEH2C*²⁶) were also identified as hits (Figures 1F and 1G).

Figure 1. Parallel CRISPRn and interference screens identify determinants of PARPi sensitivity

(A) Western blot of MCF10A *TP53*^{-/-} cell lysates illustrating expression of either doxycycline-inducible Cas9 or dCas9 fused to a KRAB transcriptional repressor (dCas9-KRAB).
 (B and C) PARPi resistance in MCF10A *TP53*^{-/-} cells. Dose-response survival curves are shown. Cells were plated in 384-well plates and exposed to PARPi for 5 days. PARPi-sensitive *BRCA1*-mutant SUM149 and PARPi-resistant *BRCA1*-revertant SUM149 cells are shown as controls. Error bars represent SD from n = 3 replicates. p values were calculated via ANOVA with Tukey’s post-test.
 (D and E) Schematics representing workflow for CRISPRn (D) and CRISPRi (E) screens.
 (F and G) Data from genome-wide CRISPRn (F) and CRISPRi (G) screens. Scatterplots are shown with olaparib vs. talazoparib drug effect Z-scores. Genes with negative Z-scores represent PARPi sensitivity-causing effects (as shown by named DNA repair genes), whereas genes with positive Z-scores represent PARPi resistance-causing effects (e.g., *PARP1*).
 (H–K) Effects of *MND1* and *PSMC3IP* compared to effects elicited via CRISPRn or CRISPRi of *BRCA1* or *BRCA2*. Plots of genome-wide drug effect Z-scores compared with gene rank product based on MaGeCK and Z score analysis from the screens described in (D) and (E).
 (L and M) *MND1* and *PSMC3IP* are highly penetrant determinants of PARPi sensitivity. Violin plots of quantile normalized Z score data (see STAR Methods) from nine different CRISPRn or CRISPRi screens for PARPi sensitivity.^{26–29} Quantile normalized Z-scores for *MND1* and *PSMC3IP* (L) or *BRCA1* and *BRCA2* (M) are highlighted. Each of the cell lines shown is a mitotic hTERT-positive/ALT-negative cell line.

Our use of both CRISPRi and CRISPRn screens, and the use of two different clinical PARPi, allowed us to identify the most profound effects that were independent of the mode of gene perturbation or the PARPi used. This approach identified two genes that encode a heterodimer classically involved in meiotic recombination, *MND1* (meiotic nuclear division protein 1 homolog) and *PSMC3IP* (PSMC3 interacting protein, *HOP2*) (Figures 1F, 1G, and S1D–S1G). We also identified *MND1* and *PSMC3IP* depletion in a retroviral mutagenesis screen for ionizing radiation (IR) sensitivity carried out in HAP1 cells (Figures S1H–S1K),³⁷ suggesting the effect of *MND1-PSMC3IP* inhibition was not specific to PARPi, but also caused sensitivity to other exogenous forms of DNA damage. When we examined each individual PARPi CRISPR-Cas9 screen, we found that the effect of targeting *MND1* or *PSMC3IP* on PARPi sensitivity was often comparable, or more profound than that achieved by CRISPR targeting of either *BRCA1* or *BRCA2* (Figures 1H–1K and S1D–S1G). We also assessed the generality of these observations by re-analysis of published CRISPR screens carried out in additional cell line backgrounds (Table S1I) and by carrying out an additional set of CRISPRn screens in another MCF10A derivative with an *RB1* tumor suppressor defect in addition to the *TP53* mutation (Figures S1L–S1N and Table S1J). CRISPR-targeting of *MND1* or *PSMC3IP* elicited PARPi sensitivity in a wider variety of cell line models than CRISPR-targeting of either *BRCA1* or *BRCA2*, suggesting that the *MND1/PARPi* and *PSMC3IP/PARPi* synthetic lethal effects had a comparably greater penetrance than the effect of targeting either *BRCA1* or *BRCA2* (Figures 1L and 1M), and that in mitotic cells, the *MND1/PSMC3IP* heterodimer might be involved in the response to PARPi.

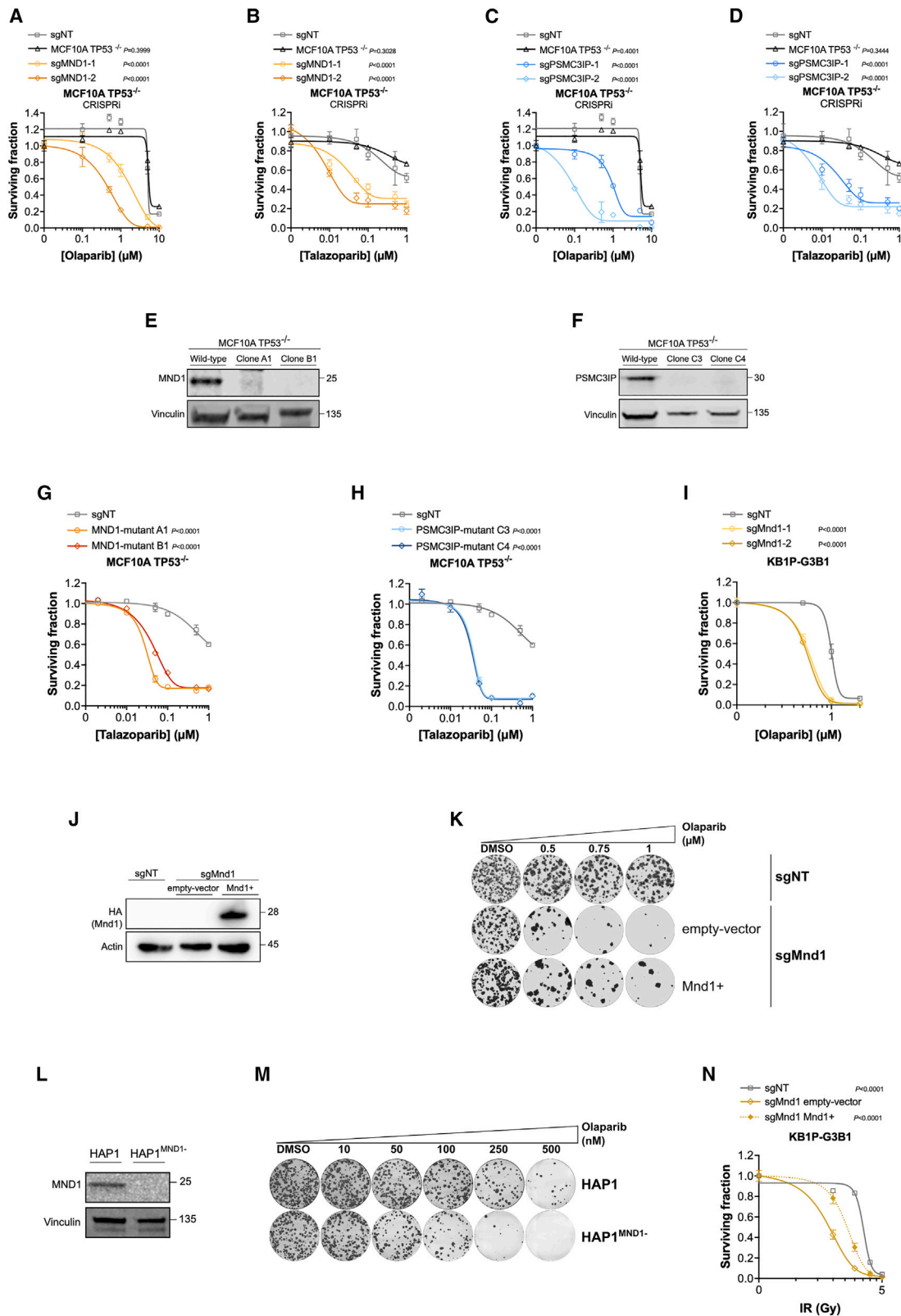
MND1 and PSMC3IP control PARPi sensitivity in mitotic cells

MND1 and *PSMC3IP* encode a DNA-binding heterodimer whose canonical function is in meiotic RAD51- or DMC1-mediated meiotic recombination.^{38,39} As part of this process, DNA double-strand DNA breaks (DSBs) are formed by SPO11. These are resected to generate exposed tracts of single-stranded DNA (ssDNA), which are in turn bound by either DMC1 or RAD51, forming a helical presynaptic nucleoprotein filament. Using RAD51/DMC1 ATPase activity, the presynaptic filament invades duplex target DNA to form a heteroduplex DNA joint (D loop), which is extended by DNA strand exchange and synthesis and then resolved to generate either cross-over or non-cross-over DNA recombinants.⁴⁰ As a part of this meiotic recombination process, the *MND1/PSMC3IP* heterodimer promotes meiotic interhomolog pairing by stabilizing the presynaptic filament and the capture of duplex DNA. The N-terminal double-stranded DNA-binding functions of *PSMC3IP/MND1* mediate synaptic complex assembly and the *PSMC3IP* C terminus binds ssDNA and stabilizes the nucleoprotein filament.⁴¹ *PSMC3IP/MND1* also regulate ATP and DNA binding by RAD51.⁴² Given this, we were interested to understand why these genes might control response to DNA-damaging agents, such as PARPi, in mitotic cells.

In addition to its role in meiotic recombination, there is some evidence that the *MND1/PSMC3IP* heterodimer also functions

in mitotic cells, which predominantly carry out HR between sister chromatids as opposed to homologous chromosomes. *MND1/PSMC3IP* are expressed in tumor cell lines, particularly those that maintain telomeres via the alternative lengthening telomeres (ALT) pathway, a form of HR.^{43,44} As part of ALT, *MND1/PSMC3IP* promotes telomere clustering and RAD51-mediated recombination between otherwise geographically distant telomeres on different chromosomes.^{43,44} To extend these observations, we analyzed gene expression and mass spectrometry proteomic data from human tumor cell lines (<https://depmap.org>) to assess the generality of *MND1/PSMC3IP* expression in mitotic cells. In human tumor cell lines, *MND1* and *PSMC3IP* mRNA and protein expression were relatively common (Figures S2A and S2B, Table S1K) and not solely restricted to tumor cell lines that carry out ALT (Figures S2C, S2D, and Tables S1K–S1N). For both *MND1* and *PSMC3IP*, mRNA expression correlated with protein expression (Figures S2E, S2F, and Tables S1K–S1N) and *MND1* expression was highly correlated with *PSMC3IP* expression (Figures S2D, S2G, Tables S1K, and S1M), consistent with the hypothesis that these two heterodimer components have a shared function in mitotic cells. Tumor expression of *MND1* and *PSMC3IP* was also relatively common (Figures S2H, S2I, and Table S1O) and highly correlated, including in those tumor types where PARPi are used clinically (breast, serous ovarian, pancreatic adenocarcinoma, and prostate adenocarcinoma; Figures S2J–S2M and Table S1O).

On the basis of our CRISPR screen results, and the data indicating that *MND1* and *PSMC3IP* are commonly expressed in mitotic tumor cells, we formally assessed whether *MND1* or *PSMC3IP* defects caused PARPi sensitivity. In CRISPRi experiments, we found that sgRNA targeting *MND1* or *PSMC3IP* enhanced sensitivity to olaparib or talazoparib (Figures 2A–2D), confirming the results of the screen. The differences in the magnitude of PARPi sensitivity demonstrated between the two *PSMC3IP* sgRNAs (Figure 2C) could be explained by the differential efficiency of the two sgRNAs to induce *PSMC3IP* silencing (Figure S3). To further validate these results, we transfected MCF10A *TP53*^{-/-} cells with Cas9-crRNA ribonucleoproteins targeting either *MND1* or *PSMC3IP* and isolated two daughter clones with different *MND1* mutations and two daughter clones with different *PSMC3IP* mutations (Figures 2E, 2F, and S4). *MND1*- or *PSMC3IP*-mutant clones were also sensitive to talazoparib (Figures 2G and 2H), a clinical PARPi known to effectively trap PARP1 on chromatin.^{7,45} This was not the case for the poor PARP1 trapper, but effective PARP1 catalytic inhibitor, veliparib (Figures S5A and S5B), suggesting that like PARPi vs. *BRCA1/2* synthetic lethality,⁴⁶ PARPi/*MND1/PSMC3IP* synthetic lethality might be more dependent on PARP1 trapping than catalytic inhibition. *MND1*- or *PSMC3IP*-mutant clones were not sensitive to a small molecule ATR inhibitor (Figures S5C and S5D), suggesting that the effect of PARPi did not necessarily extend to any agent that causes RF stress. PARPi sensitivity was not restricted to MCF10A *TP53*^{-/-} cells and was also seen in KB1P-G3B1 mouse mammary tumor cells⁴⁷ grown *ex vivo* that were CRISPR-Cas9 mutagenized by *Mnd1* sgRNA (Figures 2I, 2J, S5E, and S5F). PARPi sensitivity was also partially reversed by ectopic *Mnd1* overexpression (Figures 2K and S5G–S5I).



(legend on next page)

PARPi sensitivity was also seen in *MND1*-defective HAP1 cells (Figures 2L and 2M). We also confirmed sensitivity to IR in *MND1*- or *PSMC3IP*-mutant MCF10A *TP53*^{-/-} cells (Figures S5J and S5K) and in *Mnd1*-defective KB1P-G3B1 cells (Figure 2N). Restoration of *Mnd1* expression in *Mnd1*-defective KB1P-G3B1 cells partially reversed radiosensitivity (Figures 2N and S5L). Taken together with our prior screen data, this finding suggested that the observed PARPi synthetic lethal effects (and also IR sensitivity) were relatively common effects in mitotic cells.

PARPi sensitivity in *MND1/PSMC3IP*-defective cells is characterized by an increase in RAD51 foci and suppression of HR

The *MND1-PSMC3IP* heterodimer facilitates meiotic RAD51 function in yeast.³⁸ In cell-free *in vitro* assays, *MND1-PSMC3IP* catalyzes the binding of mouse and human RAD51 to nucleotides and DNA.⁴² The DNA lesions caused by PARPi and IR often elicit Ser-139 phosphorylation of histone variant H2AX (γ H2AX), as well as the localization of the recombinase RAD51 to the site of DNA damage.^{1,2} Using proximity ligation assays (PLAs) in mitotic KB1P-G3B1 cells, we estimated the co-localization of *Mnd1* with either Rad51 or γ H2ax. *Mnd1* co-localized with Rad51 in the presence or absence of exogenous DNA damage, as previously seen in murine and human models⁴⁸⁻⁵⁰ (Figures 3A and S6A). *Mnd1* co-localized with γ H2ax solely upon exogenous DNA damage (Figures 3B and S6B). However, when we assessed the ability of RAD51 to localize to the site of DNA damage in *MND1*-mutant MCF10A *TP53*^{-/-} cells, rather than seeing a decrease in nuclear RAD51 foci (a phenotype normally associated with an HR defect and radio or PARPi sensitivity²⁰), we observed higher levels of RAD51 foci (Figures 3C and S6C). Although the formation of Rad51 foci changed in response to

MND1/PSMC3IP loss, total levels of RAD51 did not vary to the extent that these could trivially explain the PARPi sensitivity phenotype (Figure S6D). We also saw a corresponding increase in γ H2ax foci (Figures S6C and S6E). This was also true in KB1P-G3B1 mouse mammary tumor cells with an *Mnd1* defect (Figures S7A-S7E), where the ectopic expression of *Mnd1* partially reversed this Rad51 and γ H2ax foci increase observed upon IR treatment. No difference in 53BP1 foci was detected between cells with wild-type *Mnd1*, *Mnd1* dysfunction, or cells with *Mnd1* reconstitution (Figures S7F and S7G). In *Mnd1*-defective cells, Rad51 foci were also resolved with a delayed kinetic (Figures 3D and S8A). We also noted a PARPi- or IR-induced increase of RAD51 in *PSMC3IP* mutant MCF10A *TP53*^{-/-} cells (Figures 3E, S8B, and S8C), consistent with the effects seen in *MND1* defective cells. A corresponding increase in γ H2AX foci was observed in *PSMC3IP*-mutant MCF10A *TP53*^{-/-} cells exposed to PARPi (Figures S8B and S8D). The increased RAD51 foci phenotype in *MND1*- or *PSMC3IP*-defective mitotic cells was reminiscent of the persistence of nuclear RAD51 foci in *PSMC3IP*-defective meiotic cells.⁵¹ To assess the impact of this increase in RAD51 foci on DNA repair by HR, we used a cell line with a synthetic HR reporter substrate, DR-GFP⁵² (Figure 3F). We found that either *MND1* or *PSMC3IP* gene silencing (Figures S9A and S9B) caused a decrease in HR-mediated repair (Figures 3F and S9C). Taken together, the foci and DR-GFP data suggest that RAD51 function and HR are to some extent defective in *MND1/PSMC3IP*-deficient cells.

In response to DNA damage, RAD51 has been shown to contribute to sister chromatid exchange (SCE),⁵⁵ a cross-over event that resolves Holliday junctions and shares some similarities with meiotic recombination.⁵⁶ To investigate SCE, we used HAP1 cells in which a clear increase in SCE is visible after

Figure 2. *MND1* and *PSMC3IP* defects cause PARPi and IR sensitivity in mitotic cells

(A-D) Depletion of *MND1* or *PSMC3IP* using CRISPRi sensitized MCF10A *TP53*^{-/-} cells to olaparib (A and C) and talazoparib (B and D). Dose-response survival curves are shown for MCF10A *TP53*^{-/-}dCas9-KRAB cells transduced with sgRNA targeting *MND1* (sgMND1) (A and B) or *PSMC3IP* (sgPSMC3IP) (C and D). Cells were plated in 6-well plates (A and C) or 384-well plates (B and D) and exposed to PARPi for 14 continuous days (6-well plates) or 5 continuous days (384-well plates). Error bars represent SD. p values were calculated via ANOVA with Tukey's post-test.

(E and F) Generation of *MND1*- or *PSMC3IP*-mutant clones. MCF10A *TP53*^{-/-} cells were transfected with non-targeting control or Cas9-crRNA ribonucleoproteins targeting *MND1* to generate daughter clones A1 and B1 (E) or *PSMC3IP* to generate daughter clones C3 and C4 (F). Western blot demonstrating absence of either *MND1* (E) or *PSMC3IP* (F) in lysates extracted from mutant clones. The antibodies used detect epitopes in the p.R82-E142 and p.P156-D216 regions of *MND1* and *PSMC3IP*, respectively. The targeted epitopes are C-terminal to *MND1* or *PSMC3IP* mutations generated.

(G and H) *MND1* (G) or *PSMC3IP* (H) mutant clones are more sensitive to talazoparib than wild-type cells. Dose-response survival curves are shown. Cells were plated in 384-well plates and exposed to talazoparib for 5 continuous days. Error bars represent SD from n = 3 replicates. p values were calculated via ANOVA with Tukey's post-test.

(I) *Mnd1*-defective KB1P-G3B1 cells are more sensitive to olaparib than cells expressing non-targeting control. Dose-response survival curves are shown. KB1P-G3B1 cells were transduced with lentiviral constructs encoding sgRNA targeting *Mnd1* (either sgMnd1-1 or sgMnd1-2) or non-targeting control (sgNT). Cells were plated in six-well plates and exposed to olaparib for 11 continuous days, after which colonies were stained with crystal violet. Representative image shown in Figure S5E. Error bars represent SD. p values were calculated via ANOVA with Tukey's post-test.

(J) Western blot image of KB1P-G3B1 cell lysates illustrating restoration of *Mnd1* expression via HA-tag in cells expressing a vector containing *Mnd1* cDNA (*Mnd1*⁺), but not in cells expressing empty vector. KB1P-G3B1 cells express sgRNA targeting *Mnd1* (sgMnd1) or non-targeting control (sgNT).

(K) Restoration of *Mnd1* expression (*Mnd1*⁺) in *Mnd1*-defective (sgMnd1) KB1P-G3B1 cells partially reversed olaparib sensitivity. Representative images of growth assays are shown. Cells were plated in six-well plates and exposed to olaparib for 11 continuous days, after which colonies were stained with crystal violet.

(L) Western blot demonstrating absence of *MND1* in cell lysates extracted from *MND1*-defective, but not wild-type, HAP1 cells.

(M) HAP1 cells with defective *MND1* are more sensitive to olaparib than wild-type cells. Images of clonogenic assay are shown. Cells were plated in six-well plates and exposed to olaparib for 14 continuous days.

(N) *Mnd1*-defective KB1P-G3B1 cells (sgMnd1 empty vector) are more sensitive to IR compared with cells expressing non-targeting control (sgNT). Restoration of *Mnd1* in *Mnd1*-defective KB1P-G3B1 cells (sgMnd1 *Mnd1*⁺) partially reversed radio-sensitivity. Dose-response survival curves are shown. Cells were plated in six-well plates, exposed to the indicated dose of IR and then cultured for 11 continuous days, after which colonies were stained with crystal violet. A representative image of colony formation is shown in Figure S5L. Error bars represent SD. p values were calculated via ANOVA with Tukey's post-test.

olaparib- or IR-induced DNA damage (Figures S10A–S10C). *MND1* inactivation did not alter the rates of SCEs in untreated, olaparib- or IR-exposed cells (Figures S10B and S10C). While studying SCE in the *MND1* knockout cells, we observed fewer cells with metaphase chromosomes in IR-exposed cells, suggesting that these cells do not efficiently enter mitosis. We therefore measured mitotic entry after IR-induced G_2 arrest. In contrast with *MND1* wild-type cells, only a few *MND1*-knockout HAP1 cells entered mitosis and most cells remained in the G_2 phase of the cell cycle (Figures 3G and S10D). In addition, a greater proportion of *Mnd1*-defective KP1P-G3B1 cells were in G_2/M , even in the absence of exogenous DNA damage, a phenotype that was reversed by ectopic expression of *Mnd1* (Figures S10E

and S10F). This suggested that *MND1* is required for cell cycle progression, an effect that is enhanced after DNA damage. This may be explained by an altered response of the progressing RF to DNA damage. In this context, RAD51 has been shown to mediate RF reversal in a BRCA1/2-independent fashion, a mechanism that processes stalled RFs and seems to protect cells against genotoxic stress.^{57,58} Moreover, in a BRCA1/2-dependent manner, RAD51 filament formation is required for its protective effect on the regressed arm, allowing the PARP1/RECQ1-regulated restart of reversed RFs.^{57–59} High concentrations of PARPi accelerate RF progression.⁶⁰ Based on these findings, we hypothesized that the *MND1*-PSMC3IP heterodimer contributes to RAD51 function at RFs. This prompted us

Figure 3. PARPi sensitivity in *MND1*/PSMC3IP-defective cells is characterized by an increase in RAD51 foci and suppression of HR

(A and B) *Mnd1* co-localizes with Rad51 in the presence or absence of exogenous DNA damage (A), but only co-localized with γ H2ax upon exogenous DNA damage (B). Scatterplots are shown of percentage of cells with more than five PLA foci, normalized to the total number of cells imaged in multiple ($n = 10$) fields of view. KB1P-G3B1 cells with *Mnd1* defect (sg*Mnd1*), either expressing empty vector or a vector containing *Mnd1* cDNA (*Mnd1*⁺), were plated onto coverslips. Cells were exposed to 10 Gy IR or remained unexposed. PLAs were performed after staining with anti-HA-tag (HA fused to *Mnd1*) and anti-RAD51 (A) or anti- γ H2AX (B) antibodies. Error bars represent the median and 95% confidence intervals (CIs). *p* values were calculated via ANOVA with Tukey's post-test. Representative images are shown in Figures S6A and S6B.

(C) Higher RAD51 foci levels were observed in *MND1*-mutant cells compared with wild-type cells upon olaparib or IR exposure. Scatterplot of RAD51 foci count per nucleus ($n =$ minimum of 157) in each indicated cell line is shown. MCF10A *TP53*^{-/-} cells, either wild type or with *MND1* defect (clones A1 and B1) were plated onto coverslips. Cells were either exposed to 10 μ M olaparib and then fixed after 16 h, or 10 Gy IR and then fixed after 4 h γ H2AX foci quantification in these samples is shown Figure S6E. Representative image shown in Figure S6C. Error bars represent the median and 95% CI. *p* values were calculated via ANOVA with Bonferroni's post-test.

(D) Increased Rad51 foci levels and altered kinetics of Rad51 resolution in IR-exposed *Mnd1*-mutant cells. Scatterplot of RAD51 foci count per nucleus ($n =$ minimum of 369) in each indicated cell line is shown. KB1P-G3B1 cells were plated onto coverslips, either expressing non-targeting control (sgNT) or sgRNA targeting *Mnd1* (sg*Mnd1*, expressing either empty vector or vector containing *Mnd1* cDNA (*Mnd1*⁺)). Cells were either exposed to 10 Gy IR and then fixed at the indicated time point or remained unexposed. Error bars represent the median and 95% CI. *p* values were calculated via ANOVA with Sidak's post-test. Representative images shown in Figure S8A.

(E) Higher RAD51 foci levels are observed in *PSMC3IP* mutant cells upon PARPi or IR exposure. Scatterplot of γ H2AX foci count per nucleus ($n =$ minimum of 181) in each indicated cell line is shown. MCF10A *TP53*^{-/-} cells, either wild type or with a *PSMC3IP* defect (clones C3 and C4) were plated onto coverslips. Cells were either exposed to 10 μ M olaparib and then fixed after 16 h, or 10 Gy IR and then fixed after 4 h γ H2AX foci quantification in these samples is shown in Figure S8D. Representative images shown in Figure S8B. Error bars represent the median and 95% CI. *p* values were calculated via ANOVA with Bonferroni's post-test.

(F) *MND1* or *PSMC3IP* silencing reduced HR-mediated repair. Barplot of percent GFP⁺ cells relative to cells transfected with both non-targeting control siRNA (siNT) and I-SceI is shown. Schematic of assay shown on the right. U2OS DR-GFP cells⁵² were transfected with siRNAs targeting *MND1*, *PSMC3IP*, *BRCA1*, and *BRCA2* or non-targeting control, before expression of I-SceI. A proportion of cells remained untransfected (mock) and another proportion of cells transfected with indicated siRNAs were not transfected with I-SceI for controls of background GFP positivity. GFP⁺ cells were analyzed by flow cytometry. Representative fluorescent activated cell sorter (FACS) scatterplots shown in Figure S9C.

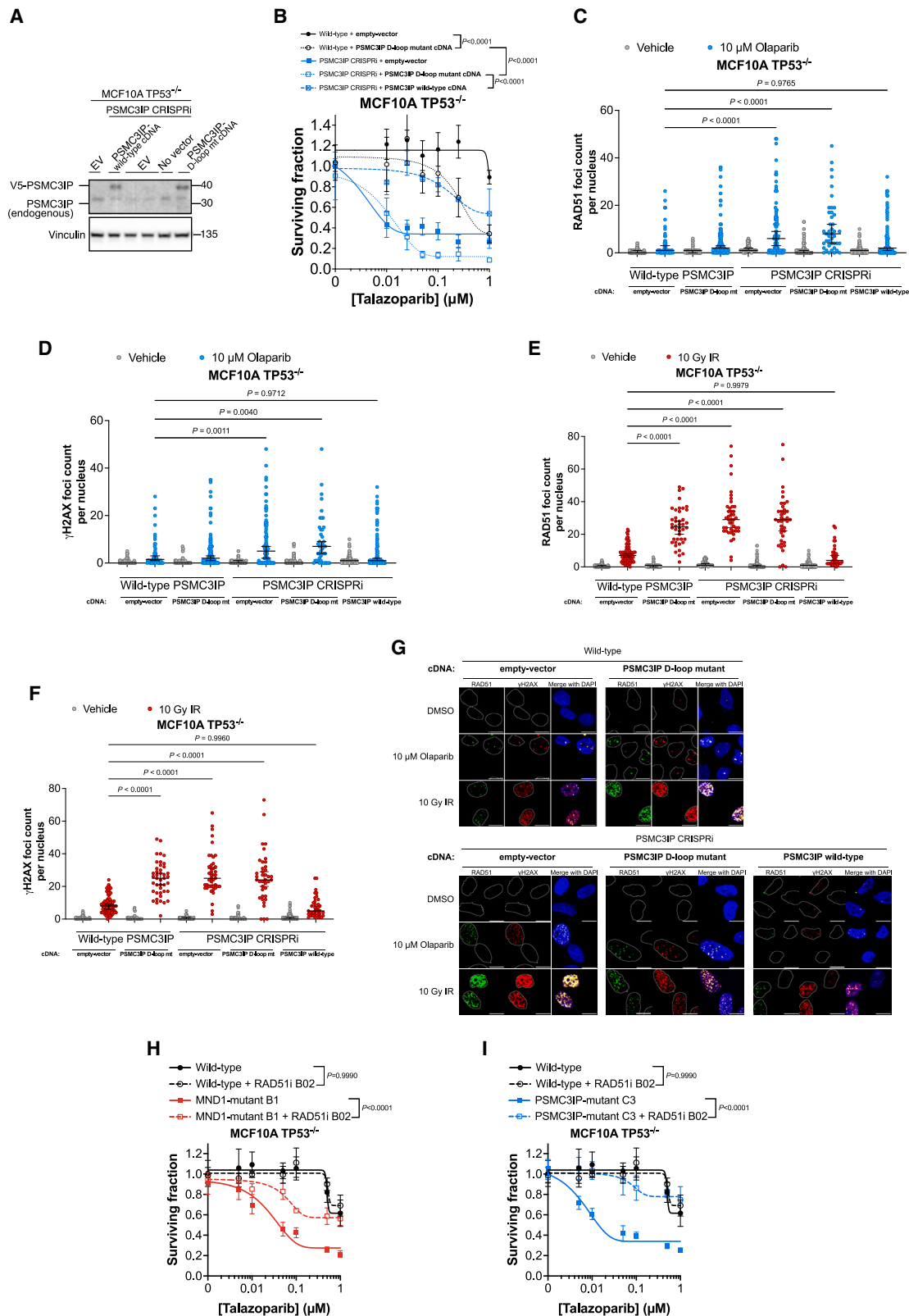
(G) *MND1* is required for cell cycle progression after DNA damage. pHistoneH3 was used as a mitotic marker.⁵³ Cells were either left untreated, exposed to 250 ng/mL nocodazole for 16 h, or exposed to 2.5 Gy IR 30 min before the 16-h nocodazole exposure. Cells were fixed and stained with propidium iodide (PI) and anti-pHistoneH3. Scatterplot of percent phospho(p)HistoneH3⁺ cells is shown. Error bars represent the median and 95% CI. *p* values were calculated via ANOVA with Dunnett's post-test. Representative FACS scatterplots shown in Figure S10D.

(H) *Mnd1* co-localizes with EdU-labelled nascent DNA, which is further increased by HU-induced RF stalling. Scatterplots of SIRF assays are shown of cells with more than PLA foci, normalized to the total number of cells imaged in multiple ($n = 15$) fields of view. KB1P-G3B1 cells with an *Mnd1* defect, either expressing empty vector or vector containing *Mnd1* cDNA (*Mnd1*⁺), were plated on coverslips with EdU. Cells were either exposed to 2 mM HU for 2 h or remained unexposed. PLAs were performed after staining with anti-HA-tag (tagged to *Mnd1*) and anti-biotin antibodies. Error bars represent the median and 95% CI. *p* values were calculated via ANOVA with Tukey's post-test. Representative images shown in Figure S10G.

(I and J) *Mnd1* is important for Brca1-independent RF degradation upon replication-blocking DNA damage. Schematic of DNA fiber assay performed in *Brca1*-deficient KB1P-G3 cells (I) and *Brca1*-proficient KB1P-G3B1 cells (J), as described in⁵⁴ with a few modifications (detailed at the top). Scatterplots showing quantification of IdU/CldU ratio of at least $n = 120$ fibers per sample (bottom). Pulse labeling followed by RF stalling via HU resulted in an increased track length ratio of *Mnd1* mutant cells (sg*Mnd1*) compared with non-targeting control (sgNT). Track length ratio was restored to wild-type levels with reconstitution of *Mnd1* cDNA (*Mnd1*⁺) (J). Error bars represent the median and 95% CI. *p* values were calculated via ANOVA with Tukey's post-test.

(K) *Mnd1* is important for RF slowing, specifically fork reversal, upon replication-blocking DNA damage. A schematic of the DNA fiber assay performed in *Brca1*-deficient KB1P-G3 cells. Scatterplot showing quantification of total track lengths of at least $n = 120$ fibers per sample (bottom). Pulse labeling followed by RF stalling via MMC resulted in increased RF progression, evidenced by increased track length, of *Mnd1* mutant (sg*Mnd1*) cells compared with non-targeting control (sgNT). Error bars represent the median and 95% CI. *p* values were calculated via ANOVA with Tukey's post-test.

(L and M) *Mnd1* loss increases micronuclei formation upon exposure to olaparib (L) or IR (M), which is reversed with ectopic *Mnd1* expression. Scatterplots of percent cells with micronuclei in each indicated sample are shown ($n = 20$). KB1P-G3B1 expressing either sgRNA targeting *Mnd1* (sg*Mnd1*) or non-targeting control (sgNT) were plated onto coverslips. *Mnd1*-deficient cells either express an empty vector or a vector containing *Mnd1* cDNA (*Mnd1*⁺). Cells were either exposed to 8 Gy IR, 10 μ M olaparib for 16 h, or remained untreated. Error bars represent the median and 95% CI. *p* values were calculated via ANOVA with Tukey's post-test. Representative images shown in Figure S11O. Scatterplots showing *Psmc3ip* loss also increases micronuclei formation upon exposure to olaparib or IR shown in Figures S11K and S11L with representative image in Figure S11R.



(legend on next page)

to test whether MND1 is present at RF using the *in situ* analysis of protein interactions at DNA RF (SIRF) assay.⁶¹ We found that Mnd1 co-localized with EdU-labelled nascent DNA in KB1P-G3B1 cells, an interaction further increased by hydroxy urea (HU)-induced RF stalling (Figures 3H and S10G). To investigate whether defective Mnd1 affects the stability of stalled RFs, we used Brca1- and Tp53-deficient KB1P-G3 cells.⁴⁷ As expected, pulse labeling with CldU and IdU followed by RF stalling using HU resulted in a significant decrease in the IdU/CldU track length ratio, indicating nucleolytic degradation of the nascent DNA of reversed RFs (Figure 3I). This was consistent with previous findings that BRCA1 stabilizes stalled forks.⁵⁹ Interestingly, the fork degradation phenotype was reversed in Mnd1-mutant cells (Figure 3I). We then investigated the effect of Mnd1 on RF stability in isogenic Brca1-proficient KB1P-G3B1 cells. Because of the presence of Brca1, a high concentration of 8 mM HU was needed to generate the RF intermediates that eventually become degraded (Figure 3J). In these cells, RF degradation was reversed by the loss of Mnd1 and then partially restored by later reconstitution with Mnd1 cDNA (Figure 3J). This suggested that the effect of MND1 on RF stalling was BRCA1 independent. A reason for the lack of HU-mediated degradation in MND1-defective cells may be a defect in RF reversal, a BRCA1/2-independent effect previously described in RAD51-deficient cells.^{58,62} Potent RAD51-dependent slowing of RF and RF reversal is achieved by MMC treatment.⁵⁷ When we exposed KB1P-G3 cells to MMC for 2 h, we observed a clear slowing of RF progression (Figure 3K). Interestingly, Mnd1 loss counteracted this fork slowing, consistent with a defect in RF reversal (Figure 3K). In fact, RF progression in Mnd1-mutant cells was slightly higher than in control cells, even in the absence of drug (Figure 3K). This suggested that MND1 is important for RF slowing upon replication-blocking DNA damage. In its absence, unrestrained RF progression may result in the accumulation of toxic DNA damage. Moreover, as Mnd1-deficient cells seemed to remain in the G₂ phase of the cell cycle (presumably to deal with persistent DNA damage), we hypothesize that the MND1-PSMC3IP heterodimer may have its major protective role in RAD51-mediated HR that does not result in cross-over events.

We then investigated whether MND1 loss is epistatic with defects in BRCA1 and BRCA2. For this purpose, we exposed Mnd1-mutated Brca1- and Tp53-deficient KB1P-G3 cells to olaparib or IR (Figures S11A–S11E). Compared with control cells and our prior observations in Brca1/Brca2 wild-type cells (Figure 2I), we did not observe further PARPi or IR sensitization when Mnd1 was CRISPR-Cas9 targeted. Mnd1 mutation in the Brca2-Tp53-deficient mouse mammary tumor cell line KB2P3.466⁶¹ also did not elicit further PARPi sensitivity (Figures S11F–S11J). This epistatic relationship was consistent with a crucial role for MND1 in HR in mitotic cells. Indeed, we found an increase in micronuclei formation in Mnd1- or Psmc3ip-deficient KB1P-G3B1 cells exposed to olaparib or IR (Figures 3L, 3M, S11K, and S11L). These micronuclei represent broken chromosome parts and not mis-segregation of whole chromosomes, as they were negative for the centromere marker CENP-B (Figures S11M–S11R). Since RAD51 nucleofilament formation is rather downstream in the HR pathway, we hypothesized that MND1 depletion should also sensitize BRCA1- and TP53-deficient cells that acquired PARPi resistance by loss of TP53BP1, which restores HR. Indeed, when we mutated Mnd1 in Brca1^{-/-} Tp53bp1^{-/-} cells, these regained olaparib sensitivity and showed increased levels of RAD51 foci upon IR or PARPi exposure (Figure S12).

Together, these data suggested that the main control of PARPi response of the MND1-PSMC3IP heterodimer in mitotic cells could be caused by a later role in HR, such as supporting RAD51-mediated D loop formation.

PARPi sensitivity is reversed by wild-type PSMC3IP but not a p.Glu201del mutant associated with female gonadal dysgenesis and a D loop defect

To functionally test the hypothesis that the MND1/PSMC3IP vs. PARPi synthetic lethal effect could be caused by a D loop defect, we made use of a previously described p.Glu201del mutant of PSMC3IP (Figure 4A). Premature truncating mutations or a deletion of p.Glu201 in PSMC3IP are associated with XX female gonadal dysgenesis (XX-GD).⁶³ Although the p.Glu201del mutation (in the C terminus of PSMC3IP) does not diminish the interaction of the MND1/PSMC3IP heterodimer with DNA, the

Figure 4. PARPi sensitivity is reversed by wild-type PSMC3IP, but not a D loop-defective p.Glu201del mutant associated with female gonadal dysgenesis

(A) Western blot of MCF10A TP53^{-/-} dCas9-KRAB cells (with or without sgRNA targeting PSMC3IP) with ectopic expression of either wild-type or p.Glu201del (D loop mutant) PSMC3IP.

(B) The PARPi-sensitivity phenotype associated with PSMC3IP defect is reversed with wild-type PSMC3IP, but not PSMC3IP p.Glu201del mutant. Dose-response survival curves are shown. Wild-type MCF10A TP53^{-/-} cells expressing PSMC3IP p.Glu201del-mutant are also more sensitive to PARPi, compared with cells expressing empty vector. MCF10A TP53^{-/-} dCas9-KRAB cells expressing non-targeting control (wild-type) or sgRNA targeting PSMC3IP (PSMC3IP CRISPRi) were transduced with lentiviral constructs encoding expression vector containing PSMC3IP cDNA, either wild-type PSMC3IP (PSMC3IP wild-type cDNA) or PSMC3IP p.Glu201del (PSMC3IP D loop mutant cDNA). Cells were plated in 96-well plates and exposed to talazoparib for ten continuous days. Error bars represent SD from n = 3 replicates. p values were calculated via ANOVA with Tukey's post-test.

(C–G) Higher RAD51 (C and E) and γH2AX (D and F) foci levels were observed in PSMC3IP CRISPRi cells compared with wild-type upon olaparib (C and D) or IR (E and F) exposure, which was partially reversed with expression of wild-type PSMC3IP, but not PSMC3IP p.Glu201del D loop mutant. Cells were plated onto coverslips and either exposed to 10 μM olaparib and then fixed after 16 h or 10 Gy IR and then fixed after 4 h. Scatterplot of RAD51 or γH2AX foci count per nucleus (n = minimum of 41) in each indicated cell line is shown in C–F. Error bars represent the median and 95% CI. p values were calculated via ANOVA with Bonferroni's post-test. Representative images are shown in G. Scale bar, 10 μm.

(H and I) RAD51 inhibition reverses the PARPi sensitivity phenotype in both MND1 (H) and PSMC3IP (I) mutant cells. Dose-response survival curves are shown. Cells were plated in 384-well plates and exposed to 25-μM small molecule RAD51 inhibitor B02 for 1 h before talazoparib addition. Cells were then exposed to PARPi for continuous days. Cell viability was quantified by CellTiter-Glo. Error bars represent SD from n = 3 replicates. p values were calculated via ANOVA with Tukey's post-test.

interaction with RAD51 is impaired, as is the ability to promote D loop formation.⁶⁴ Although ectopic expression of wild-type *PSMC3IP* reversed PARPi sensitivity in these cells (Figures 4A and 4B), the expression of a p.Glu201del-mutant version of *PSMC3IP* did not; in fact, expression of the p.Glu201del mutant further sensitized cells to PARPi (Figures 4A and 4B). Expression of the *PSMC3IP* p.Glu201del mutant also sensitized *PSMC3IP* wild-type MCF10A *TP53*^{-/-} cells to PARPi (Figures 4A and 4B), consistent with this mutation acting in a dominant-negative fashion.⁶⁴ Although this remains to be formally assessed, one hypothesis is that it is loss of either the RAD51 interaction and/or the inability to promote D loop formation is the cause of PARPi sensitivity in *PSMC3IP*-defective cells. Consistent with our aforementioned observation that PARPi sensitivity in *PSMC3IP* mutant cells is associated with an increase in RAD51 foci, the expression of *PSMC3IP* p.Glu201del resulted in increased RAD51 foci formation upon IR or PARPi exposure (Figures 4C–4G). This was true for *PSMC3IP*-depleted cells as well as in cells with wild-type *PSMC3IP*. Ectopic expression of wild-type *PSMC3IP* reversed the RAD51 foci phenotype in *PSMC3IP*-depleted cells, establishing a causal relationship (Figures 4C–4G). We therefore surmised that the increased RAD51 nucleoprotein formation in *MND1*- and *PSMC3IP*-mutant cells exposed to PARPi might be the key cytotoxic event. Consistent with this, the inhibition of RAD51 with the previously described RAD51 inhibitor B02, which inhibits the single- and double-stranded DNA binding and strand exchange activity of RAD51,^{65,66} partially reversed the PARPi sensitivity phenotype in both *MND1*- and *PSMC3IP*-mutant cells (Figures 4H, 4I, and S13).

DISCUSSION

Our data are consistent with a role for the *PSMC3IP*-*MND1* heterodimer in controlling RAD51 nucleofilament-mediated D loop formation in mitotic cells, in addition to their role in inter-chromosomal recombination in meiotic cells. Some evidence that the *MND1*-*PSMC3IP* heterodimer also functions in mitotic cells came from the observation that these proteins contribute to ALT,^{43,44} where the *MND1*-*PSMC3IP* heterodimer promotes telomere clustering and RAD51-mediated recombination between distant telomeres. Our data show that both *MND1* and *PSMC3IP* are also expressed in mitotic cells, which do not use ALT. Hence, the *MND1*-*PSMC3IP* heterodimer seems to have a more general supportive role of RAD51-associated functions in mitotic cells.

We found that *PSMC3IP*- or *MND1*-deficient cells have a profound PARPi sensitivity. The inactivation of *Mnd1* in *Brca1*- or *Brca2*-deficient cells did not further increase PARPi sensitivity, consistent with an epistatic role in the HR pathway. An important difference from *BRCA1/2* defects is that cells lacking *PSMC3IP* or *MND1* function have persisting RAD51 foci formation after DNA damage. In contrast, *BRCA1/2*-mutant cells do not form RAD51 foci and the lack of RAD51 foci formation is used as a surrogate marker for HR deficiency and to predict PARPi response.^{18–20} Here, we present an example of prolonged RAD51 foci formation, which is also an outcome of dysfunctional HR. This suggests that, as well as assessing the loss of RAD51 foci in order to predict PARPi sensitivity, assessing the kinetics

of RAD51 foci formation and resolution might also be important, as prolonged RAD51 foci formation may also indicate HR defects. It would be interesting to investigate whether this phenotype can be observed in the tumors of patients that respond to PARPi, despite the presence of RAD51 foci.

MND1-deficient cells also exhibited a defect in RF slowing after DNA damage. This is consistent with a contribution of *MND1* to RF reversal, another RAD51-associated function.^{58,62} In the absence of RF slowing after DNA damage, unrestrained RF progression may increase the amount of DNA damage, including DSBs. The HR-mediated repair of DSBs is clearly a major function that both *MND1* and *PSMC3IP* have in mitotic cells. Within the HR pathway, we conclude that impaired D loop formation could be responsible for the HR defect and toxic RAD51 foci formation. This is based on our experiments using the p.Glu201del mutant of *PSMC3IP*, a mutation that does not alter the interaction of the *MND1*-*PSMC3IP* heterodimer with DNA but does impair the interaction with RAD51 and its ability to promote D loop formation.⁶⁴ In contrast with wild-type *PSMC3IP*, the p.Glu201del mutant does not rescue PARPi-induced prolonged RAD51 foci formation and PARPi sensitivity. These conclusions are strengthened by our experiments demonstrating rescue of PARPi sensitivity of *PSMC3IP*-defective cells using small molecule RAD51 inhibitor, B02, which specifically inhibits single- and double-stranded DNA binding and strand exchange activity of RAD51. Interestingly, this RAD51 inhibitor has been previously shown to increase PARPi sensitivity of HR-proficient triple-negative breast cancer (TNBC) cell lines, but not HR-proficient non-TNBC cell lines, such as MCF10A, which is the main breast-relevant model used in this study.⁶⁷

Overall, our data contribute to the mechanistic insight to our understanding of how PARPi response is controlled and how *MND1*-*PSMC3IP* regulate the response to DNA damage in mitotic cells, outside of their role in ALT.

Limitations of the study

One limitation of our study is that we are unable to conclusively state whether *MND1*/*PSMC3IP* defects cause an increase in DNA lesions, or whether *MND1*/*PSMC3IP* defects cause an inability to resolve a RAD51 nucleoprotein filament. However, we have settled on a model where *MND1*/*PSMC3IP* defects do not themselves cause a profound increase in DNA lesions that require RAD51 for repair but, in cells exposed to PARPi, the lack of *MND1*/*PSMC3IP* causes the formation of toxic RAD51 (i.e., failure to remove RAD51). This is for a number of reasons. For example, in *MND1*/*PSMC3IP*-defective cells cultured in the absence of PARPi, we did not see a detectable increase in RAD51 foci (Figures 3C and 3E) or a consistent increase in γ H2AX or 53BP1 foci (Figures S6E, S8D, S7F, and S7G). Second, we were able to partially reverse the *MND1*/*PSMC3IP* vs. PARPi synthetic lethality by using a small molecule that disrupts the interface between individual RAD51 monomers when arranged on a nucleoprotein filament (Figures 4H and 4I). However, we acknowledge that we cannot fully exclude other models, such as one where the *MND1*/*PSMC3IP* defect itself causes DNA lesions to form that are repaired by PARP1. Such DNA damage might be at a level below the sensitivity of a γ H2AX or 53BP1 assay, for example.

We noted that ectopic expression of Mnd1 in Mnd1 defective cells caused a partial restoration of olaparib resistance (Figure 2K) and IR resistance (Figure 2N), as well as partial reversal of the RAD51 phenotype (Figure 3D). One explanation for failing to fully reverse these phenotypes could be that ectopic expression of genes, such as Mnd1, rarely recapitulates native expression in terms of total amounts as well as temporal or spatial expression.

In addition, we note that we did not show a loss of Mnd1 protein expression in the experiments carried out in mouse cells. Although we tested all commercially available MND1 antibodies to identify one that detected murine Mnd1, we were unable to identify one that produced a specific Mnd1 signal at the relevant molecular weight. We did, however, demonstrate that the Mnd1 qRT-PCR signal was decreased by CRISPR targeting of Mnd1 and that this decrease was reversed by ectopic expression of Mnd1 cDNA (Figure S5G), suggesting that endogenous Mnd1 is inactivated by CRISPR targeting in mouse cells.

STAR★METHODS

Detailed methods are provided in the online version of this paper and include the following:

- KEY RESOURCES TABLE
- RESOURCE AVAILABILITY
 - Lead contact
 - Materials availability
 - Data and code availability
- EXPERIMENTAL MODEL AND SUBJECT DETAILS
 - Cell lines
 - Reagents
- METHOD DETAILS
 - Western blotting
 - Haploid genetic screens
 - CRISPR screens
 - Gene editing and silencing, plasmids, and cloning
 - *In vitro* cell survival assays
 - RAD51 and γ H2AX immunofluorescence assays
 - Single-molecule DNA fiber assay
 - Analysis of micronuclei formation
 - Flow cytometric analysis
 - Proximity ligation assay (PLA)
 - *In situ* analysis of protein interactions at DNA replication forks (SIRF)
 - Sister chromatid exchange assay
 - G2-arrest analysis
 - qRT-PCR
- QUANTIFICATION AND STATISTICAL ANALYSIS

SUPPLEMENTAL INFORMATION

Supplemental information can be found online at <https://doi.org/10.1016/j.celrep.2023.112484>.

ACKNOWLEDGMENTS

We thank Jeremy Stark (City of Hope) for the kind gift of U2OS-DR-GFP cells and Thijn Brummelkamp (NKI) for providing HAP1 cells. This work was funded by the Swiss National Science Foundation (310030_179360 to R.S.R.), the Eu-

ropean Research Council (CoG-681572 to S.S.R.), the Swiss Cancer League (KLS-4282-08-2017 to S.R.), the Wilhelm Sander Foundation (no. 2019.069.1 to S.R.), Breast Cancer Now (as part of Program Funding to C.J.L. and A.N.J.T. as part of the Breast Cancer Now Toby Robins Research Centre), and Cancer Research UK (as part of Program Funding to S.J.P. and C.J.L.). We also thank Breast Cancer Now Toby Robins Research Center Bioinformatics Core for Bioinformatics Support and thank Breast Cancer Now, working in partnership with Walk the Walk for supporting the work of this team. We also thank Dr. Kai Betteridge and their team in the ICR Light Microscopy Facility for assistance with microscopy. This work represents independent research supported by the National Institute for Health Research (NIHR) Biomedical Research Center at The Royal Marsden NHS Foundation Trust and the Institute of Cancer Research, London. The views expressed are those of the author(s) and not necessarily those of the NIHR or the Department of Health and Social Care.

AUTHOR CONTRIBUTIONS

A.Z., conceptualization, data curation, formal analysis, validation, investigation, methodology, writing – original draft, writing – review and editing. P.F., conceptualization, data curation, formal analysis, validation, investigation, methodology, writing – original draft, writing – review and editing. L.L., M.M., C.S., J.S.B., M.L., J.A., R.B., A.G., S.H., M.R., F.S., S.S., data curation and formal analysis. J.V.F., M.J.O., B.R.D., and M.A.T.M.v.V., experimental methodology and reagent provision. D.B.K., data curation, formal analysis, supervision, writing, and editing. S.J.P., A.N.J.T., S.R., C.J.L., conceptualization, resources, supervision, funding acquisition, investigation, writing – original draft, revision, and editing.

DECLARATION OF INTERESTS

C.J.L. makes the following disclosures: receives and/or has received research funding from AstraZeneca, Merck KGaA, and Artios; received consultancy, SAB membership, or honoraria payments from Syncona, Sun Pharma, Gerson Lehrman Group, Merck KGaA, Vertex, AstraZeneca, Tango, 3rd Rock, Ono Pharma, Artios, Abingworth, Tesselate, and Dark Blue Therapeutics; has stock in Tango, Ovibio, Enebra Tx., Hysplex, and Tesselate. C.J.L. is also a named inventor on patents describing the use of DNA repair inhibitors, stands to gain from their development and use as part of the ICR “Rewards to Inventors” scheme, and also reports benefits from this scheme associated with patents for PARP inhibitors paid into C.J.L.’s personal account and research accounts at the Institute of Cancer Research. A.N.J.T. reports personal honoraria from Pfizer, Vertex, Prime Oncology, Artios, MD Anderson, Medscape Education, EM Partners, GBCC conference, Cancer Panel, and Research to Practise; honoraria to either the Institute of Cancer Research or King’s College research accounts from SABCS, VJ Oncology, GE Healthcare, Gilead, AZ ESMO symposium, IBCS conference, and AstraZeneca Ad boards; received honoraria and stock in InBioMotion; honoraria and financial support for research from AstraZeneca, Medivation, Myriad Genetics, and Merck Serono; and travel expenses covered by AstraZeneca for any trial-related meetings or trial commitments abroad. A.N.J.T. reports benefits from ICR’s Inventors Scheme associated with patents for PARP inhibitors in BRCA1/2-associated cancers, paid into research accounts at the Institute of Cancer Research and to A.N.J.T.’s personal account. J.V.F., M.O.C., and B.R.D. are full-time employees and shareholders at AstraZeneca.

Received: September 2, 2022

Revised: December 22, 2022

Accepted: April 24, 2023

Published: May 9, 2023

REFERENCES

1. Bryant, H.E., Schultz, N., Thomas, H.D., Parker, K.M., Flower, D., Lopez, E., Kyle, S., Meuth, M., Curtin, N.J., and Helleday, T. (2005). Specific killing of BRCA2-deficient tumours with inhibitors of poly(ADP-ribose) polymerase. *Nature* 434, 913–917. <https://doi.org/10.1038/nature03443>.

2. Farmer, H., McCabe, N., Lord, C.J., Tutt, A.N.J., Johnson, D.A., Richardson, T.B., Santarosa, M., Dillon, K.J., Hickson, I., Knights, C., et al. (2005). Targeting the DNA repair defect in BRCA mutant cells as a therapeutic strategy. *Nature* 434, 917–921. <https://doi.org/10.1038/nature03445>.
3. Robson, M., Im, S.A., Senkus, E., Xu, B., Domchek, S.M., Masuda, N., Delaloge, S., Li, W., Tung, N., Armstrong, A., et al. (2017). Olaparib for metastatic breast cancer in patients with a germline BRCA mutation. *N. Engl. J. Med.* 377, 523–533. <https://doi.org/10.1056/NEJMoa1706450>.
4. Litton, J.K., Rugo, H.S., Ettl, J., Hurvitz, S.A., Gonçalves, A., Lee, K.H., Fehrenbacher, L., Yerushalmi, R., Mina, L.A., Martin, M., et al. (2018). Talazoparib in patients with advanced breast cancer and a germline BRCA mutation. *N. Engl. J. Med.* 379, 753–763. <https://doi.org/10.1056/NEJMoa1802905>.
5. Kaelin, W.G., Jr. (2005). The concept of synthetic lethality in the context of anticancer therapy. *Nat. Rev. Cancer* 5, 689–698. <https://doi.org/10.1038/nrc1691>.
6. Murai, J., Huang, S.Y.N., Das, B.B., Renaud, A., Zhang, Y., Doroshow, J.H., Ji, J., Takeda, S., and Pommier, Y. (2012). Trapping of PARP1 and PARP2 by clinical PARP inhibitors. *Cancer Res.* 72, 5588–5599. <https://doi.org/10.1158/0008-5472.CAN-12-2753>.
7. Krastev, D.B., Wicks, A.J., and Lord, C.J. (2021). PARP inhibitors - trapped in a toxic love affair. *Cancer Res.* 81, 5605–5607. <https://doi.org/10.1158/0008-5472.CAN-21-3201>.
8. Hanzlikova, H., Kalasova, I., Demin, A.A., Pennicott, L.E., Cihlarova, Z., and Caldecott, K.W. (2018). The importance of poly(ADP-ribose) polymerase as a sensor of unligated Okazaki fragments during DNA replication. *Mol. Cell* 71, 319–331.e3. <https://doi.org/10.1016/j.molcel.2018.06.004>.
9. Vaitsiankova, A., Burdova, K., Sobol, M., Gautam, A., Benada, O., Hanzlikova, H., and Caldecott, K.W. (2022). PARP inhibition impedes the maturation of nascent DNA strands during DNA replication. *Nat. Struct. Mol. Biol.* 29, 329–338. <https://doi.org/10.1038/s41594-022-00747-1>.
10. Cong, K., Peng, M., Kousholt, A.N., Lee, W.T.C., Lee, S., Nayak, S., Kraiss, J., VanderVere-Carozza, P.S., Pawelczak, K.S., Calvo, J., et al. (2021). Replication gaps are a key determinant of PARP inhibitor synthetic lethality with BRCA deficiency. *Mol. Cell* 81, 3128–3144.e7. <https://doi.org/10.1016/j.molcel.2021.06.011>.
11. Dréan, A., Williamson, C.T., Brough, R., Brandsma, I., Menon, M., Konde, A., Garcia-Murillas, I., Pemberton, H.N., Frankum, J., Rafiq, R., et al. (2017). Modeling therapy resistance in BRCA1/2-mutant cancers. *Mol. Cancer Therapeut.* 16, 2022–2034. <https://doi.org/10.1158/1535-7163.MCT-17-0098>.
12. Cancer Genome Atlas Research Network (2011). Integrated genomic analyses of ovarian carcinoma. *Nature* 474, 609–615. <https://doi.org/10.1038/nature10166>.
13. Ledermann, J., Harter, P., Gourley, C., Friedlander, M., Vergote, I., Rustin, G., Scott, C., Meier, W., Shapira-Frommer, R., Safra, T., et al. (2012). Olaparib maintenance therapy in platinum-sensitive relapsed ovarian cancer. *N. Engl. J. Med.* 366, 1382–1392. <https://doi.org/10.1056/NEJMoa1105535>.
14. Davies, H., Glodzik, D., Morganella, S., Yates, L.R., Staaf, J., Zou, X., Ramakrishna, M., Martin, S., Boyault, S., Sieuwerts, A.M., et al. (2017). HRDetect is a predictor of BRCA1 and BRCA2 deficiency based on mutational signatures. *Nat. Med.* 23, 517–525. <https://doi.org/10.1038/nm.4292>.
15. Gulhan, D.C., Lee, J.J.K., Melloni, G.E.M., Cortés-Ciriano, I., and Park, P.J. (2019). Detecting the mutational signature of homologous recombination deficiency in clinical samples. *Nat. Genet.* 51, 912–919. <https://doi.org/10.1038/s41588-019-0390-2>.
16. Polak, P., Kim, J., Braunstein, L.Z., Karlic, R., Haradhavala, N.J., Tiao, G., Rosebrock, D., Livitz, D., Kübler, K., Mouw, K.W., et al. (2017). A mutational signature reveals alterations underlying deficient homologous recombination repair in breast cancer. *Nat. Genet.* 49, 1476–1486. <https://doi.org/10.1038/ng.3934>.
17. Nik-Zainal, S., Davies, H., Staaf, J., Ramakrishna, M., Glodzik, D., Zou, X., Martincorena, I., Alexandrov, L.B., Martin, S., Wedge, D.C., et al. (2016). Landscape of somatic mutations in 560 breast cancer whole-genome sequences. *Nature* 534, 47–54. <https://doi.org/10.1038/nature17676>.
18. Cruz, C., Castroviejo-Bermejo, M., Gutiérrez-Enríquez, S., Llop-Guevara, A., Ibrahim, Y.H., Gris-Oliver, A., Bonache, S., Morancho, B., Bruna, A., Rueda, O.M., et al. (2018). RAD51 foci as a functional biomarker of homologous recombination repair and PARP inhibitor resistance in germline BRCA-mutated breast cancer. *Ann. Oncol.* 29, 1203–1210. <https://doi.org/10.1093/annonc/ndy099>.
19. Llop-Guevara, A., Loibl, S., Villacampa, G., Vladimirova, V., Schneeweiss, A., Kam, T., Zahm, D.M., Herencia-Roper, A., Jank, P., van Mackelenbergh, M., et al. (2021). Association of RAD51 with homologous recombination deficiency (HRD) and clinical outcomes in untreated triple-negative breast cancer (TNBC): analysis of the GeparSixto randomized clinical trial. *Ann. Oncol.* 32, 1590–1596. <https://doi.org/10.1016/j.annonc.2021.09.003>.
20. van Wijk, L.M., Vermeulen, S., Meijers, M., van Diest, M.F., Ter Haar, N.T., de Jonge, M.M., Solleveld-Westerink, N., van Wezel, T., van Gent, D.C., Kroep, J.R., et al. (2020). The RECAP test rapidly and reliably identifies homologous recombination-deficient ovarian carcinomas. *Cancers* 12, 2805. <https://doi.org/10.3390/cancers12102805>.
21. Hakem, R., de la Pompa, J.L., Elia, A., Potter, J., and Mak, T.W. (1997). Partial rescue of Brca1 (5-6) early embryonic lethality by p53 or p21 null mutation. *Nat. Genet.* 16, 298–302. <https://doi.org/10.1038/ng0797-298>.
22. Hakem, R., de la Pompa, J.L., Sirard, C., Mo, R., Woo, M., Hakem, A., Wakeham, A., Potter, J., Reitmair, A., Billia, F., et al. (1996). The tumor suppressor gene Brca1 is required for embryonic cellular proliferation in the mouse. *Cell* 85, 1009–1023. [https://doi.org/10.1016/s0092-8674\(00\)81302-1](https://doi.org/10.1016/s0092-8674(00)81302-1).
23. Ludwig, T., Chapman, D.L., Papaioannou, V.E., and Efstratiadis, A. (1997). Targeted mutations of breast cancer susceptibility gene homologs in mice: lethal phenotypes of Brca1, Brca2, Brca1/Brca2, Brca1/p53, and Brca2/p53 nullizygous embryos. *Genes Dev.* 11, 1226–1241. <https://doi.org/10.1101/gad.11.10.1226>.
24. Gossen, M., and Bujard, H. (1992). Tight control of gene expression in mammalian cells by tetracycline-responsive promoters. *Proc. Natl. Acad. Sci. USA* 89, 5547–5551. <https://doi.org/10.1073/pnas.89.12.5547>.
25. Bajrami, I., Frankum, J.R., Konde, A., Miller, R.E., Rehman, F.L., Brough, R., Campbell, J., Sims, D., Rafiq, R., Hooper, S., et al. (2014). Genome-wide profiling of genetic synthetic lethality identifies CDK12 as a novel determinant of PARP1/2 inhibitor sensitivity. *Cancer Res.* 74, 287–297. <https://doi.org/10.1158/0008-5472.CAN-13-2541>.
26. Zimmermann, M., Murina, O., Reijns, M.A.M., Agathangelou, A., Challis, R., Tarnauskaitė, Ž., Muir, M., Fluteau, A., Aregger, M., McEwan, A., et al. (2018). CRISPR screens identify genomic ribonucleotides as a source of PARP-trapping lesions. *Nature* 559, 285–289. <https://doi.org/10.1038/s41586-018-0291-z>.
27. Clements, K.E., Schleicher, E.M., Thakar, T., Hale, A., Dhoonmoon, A., Tolman, N.J., Sharma, A., Liang, X., Imamura Kawasawa, Y., Nicolae, C.M., et al. (2020). Identification of regulators of poly-ADP-ribose polymerase inhibitor response through complementary CRISPR knockout and activation screens. *Nat. Commun.* 11, 6118. <https://doi.org/10.1038/s41467-020-19961-w>.
28. DeWeirdt, P.C., Sangree, A.K., Hanna, R.E., Sanson, K.R., Hegde, M., Strand, C., Persky, N.S., and Doench, J.G. (2020). Genetic screens in isogenic mammalian cell lines without single cell cloning. *Nat. Commun.* 11, 752. <https://doi.org/10.1038/s41467-020-14620-6>.
29. Olivieri, M., Cho, T., Álvarez-Quilón, A., Li, K., Schellenberg, M.J., Zimmermann, M., Hustedt, N., Rossi, S.E., Adam, S., Melo, H., et al. (2020). A genetic map of the response to DNA damage in human cells. *Cell* 182, 481–496.e21. <https://doi.org/10.1016/j.cell.2020.05.040>.
30. Tzelepis, K., Koike-Yusa, H., De Braekeleer, E., Li, Y., Metzakopian, E., Dovey, O.M., Mupo, A., Grinkevich, V., Li, M., Mazan, M., et al. (2016). A CRISPR dropout screen identifies genetic vulnerabilities and therapeutic targets in acute myeloid leukemia. *Cell Rep.* 17, 1193–1205. <https://doi.org/10.1016/j.celrep.2016.09.079>.

31. Colic, M., Wang, G., Zimmermann, M., Mascall, K., McLaughlin, M., Bertollet, L., Lenoir, W.F., Moffat, J., Angers, S., Durocher, D., and Hart, T. (2019). Identifying chemogenetic interactions from CRISPR screens with drugZ. *Genome Med.* *11*, 52. <https://doi.org/10.1186/s13073-019-0665-3>.
32. Hart, T., Brown, K.R., Sircoulomb, F., Rottapel, R., and Moffat, J. (2014). Measuring error rates in genomic perturbation screens: gold standards for human functional genomics. *Mol. Syst. Biol.* *10*, 733. <https://doi.org/10.15252/msb.20145216>.
33. Horlbeck, M.A., Gilbert, L.A., Villalta, J.E., Adamson, B., Pak, R.A., Chen, Y., Fields, A.P., Park, C.Y., Corn, J.E., Kampmann, M., and Weissman, J.S. (2016). Compact and highly active next-generation libraries for CRISPR-mediated gene repression and activation. *Elife* *5*, e19760. <https://doi.org/10.7554/eLife.19760>.
34. Pettitt, S.J., Krastev, D.B., Brandsma, I., Dréan, A., Song, F., Aleksandrov, R., Harrell, M.I., Menon, M., Brough, R., Campbell, J., et al. (2018). Genome-wide and high-density CRISPR-Cas9 screens identify point mutations in PARP1 causing PARP inhibitor resistance. *Nat. Commun.* *9*, 1849. <https://doi.org/10.1038/s41467-018-03917-2>.
35. McCabe, N., Turner, N.C., Lord, C.J., Kluzek, K., Bialkowska, A., Swift, S., Giavara, S., O'Connor, M.J., Tutt, A.N., Zdzienicka, M.Z., et al. (2006). Deficiency in the repair of DNA damage by homologous recombination and sensitivity to poly(ADP-ribose) polymerase inhibition. *Cancer Res.* *66*, 8109–8115. <https://doi.org/10.1158/0008-5472.CAN-06-0140>.
36. Jamal, K., Galbiati, A., Armenia, J., Illuzzi, G., Hall, J., Bentouati, S., Barrell, D., Ahdesmäki, M., O'Connor, M.J., Leo, E., and Forment, J.V. (2022). Drug-gene interaction screens coupled to tumour data analyses identify the most clinically-relevant cancer vulnerabilities driving sensitivity to PARP inhibition. Preprint at bioRxiv. <https://doi.org/10.1101/2022.07.29.501846>.
37. Francica, P., Mutlu, M., Blomen, V.A., Oliveira, C., Nowicka, Z., Trenner, A., Gerhards, N.M., Bouwman, P., Stickel, E., Hekkelman, M.L., et al. (2020). Functional radiogenetic profiling implicates ERCC6L2 in non-homologous end joining. *Cell Rep.* *32*, 108068. <https://doi.org/10.1016/j.celrep.2020.108068>.
38. Tsubouchi, H., and Roeder, G.S. (2002). The Mnd1 protein forms a complex with hop2 to promote homologous chromosome pairing and meiotic double-strand break repair. *Mol. Cell Biol.* *22*, 3078–3088. <https://doi.org/10.1128/MCB.22.9.3078-3088.2002>.
39. Chen, Y.K., Leng, C.H., Olivares, H., Lee, M.H., Chang, Y.C., Kung, W.M., Ti, S.C., Lo, Y.H., Wang, A.H.J., Chang, C.S., et al. (2004). Heterodimeric complexes of Hop2 and Mnd1 function with Dmc1 to promote meiotic homologous juxtaposition and strand assimilation. *Proc. Natl. Acad. Sci. USA* *101*, 10572–10577. <https://doi.org/10.1073/pnas.0404195101>.
40. Crickard, J.B., and Greene, E.C. (2018). Biochemical attributes of mitotic and meiotic presynaptic complexes. *DNA Repair* *71*, 148–157. <https://doi.org/10.1016/j.dnarep.2018.08.018>.
41. Zhao, W., Saro, D., Hammel, M., Kwon, Y., Xu, Y., Rambo, R.P., Williams, G.J., Chi, P., Lu, L., Pezza, R.J., et al. (2014). Mechanistic insights into the role of Hop2-Mnd1 in meiotic homologous DNA pairing. *Nucleic Acids Res.* *42*, 906–917. <https://doi.org/10.1093/nar/gkt924>.
42. Bugreev, D.V., Huang, F., Mazina, O.M., Pezza, R.J., Voloshin, O.N., Camerini-Otero, R.D., and Mazin, A.V. (2014). HOP2-MND1 modulates RAD51 binding to nucleotides and DNA. *Nat. Commun.* *5*, 4198. <https://doi.org/10.1038/ncomms5198>.
43. Dilley, R.L., Verma, P., Cho, N.W., Winters, H.D., Wondisford, A.R., and Greenberg, R.A. (2016). Break-induced telomere synthesis underlies alternative telomere maintenance. *Nature* *539*, 54–58. <https://doi.org/10.1038/nature20099>.
44. Cho, N.W., Dilley, R.L., Lampson, M.A., and Greenberg, R.A. (2014). Interchromosomal homology searches drive directional ALT telomere movement and synapsis. *Cell* *159*, 108–121. <https://doi.org/10.1016/j.cell.2014.08.030>.
45. Murai, J., Huang, S.Y.N., Renaud, A., Zhang, Y., Ji, J., Takeda, S., Morris, J., Teicher, B., Doroshow, J.H., and Pommier, Y. (2014). Stereospecific PARP trapping by BMN 673 and comparison with olaparib and rucaparib. *Mol. Cancer Therapeut.* *13*, 433–443. <https://doi.org/10.1158/1535-7163.MCT-13-0803>.
46. Shen, Y., Rehman, F.L., Feng, Y., Boshuizen, J., Bajrami, I., Elliott, R., Wang, B., Lord, C.J., Post, L.E., and Ashworth, A. (2013). BMN 673, a novel and highly potent PARP1/2 inhibitor for the treatment of human cancers with DNA repair deficiency. *Clin. Cancer Res.* *19*, 5003–5015. <https://doi.org/10.1158/1078-0432.CCR-13-1391>.
47. Barazas, M., Gasparini, A., Huang, Y., Küçükosmanoğlu, A., Annunziato, S., Bouwman, P., Sol, W., Kersbergen, A., Proost, N., de Korte-Grimmerink, R., et al. (2019). Radiosensitivity is an acquired vulnerability of PARP1-resistant BRCA1-deficient tumors. *Cancer Res.* *79*, 452–460. <https://doi.org/10.1158/0008-5472.CAN-18-2077>.
48. Petukhova, G.V., Pezza, R.J., Vanevski, F., Ploquin, M., Masson, J.Y., and Camerini-Otero, R.D. (2005). The Hop2 and Mnd1 proteins act in concert with Rad51 and Dmc1 in meiotic recombination. *Nat. Struct. Mol. Biol.* *12*, 449–453. <https://doi.org/10.1038/nsmb923>.
49. Pezza, R.J., Petukhova, G.V., Ghirlando, R., and Camerini-Otero, R.D. (2006). Molecular activities of meiosis-specific proteins Hop2, Mnd1, and the Hop2-Mnd1 complex. *J. Biol. Chem.* *281*, 18426–18434. <https://doi.org/10.1074/jbc.M601073200>.
50. Chi, P., San Filippo, J., Sehorn, M.G., Petukhova, G.V., and Sung, P. (2007). Bipartite stimulatory action of the Hop2-Mnd1 complex on the Rad51 recombinase. *Genes Dev.* *21*, 1747–1757. <https://doi.org/10.1101/gad.1563007>.
51. Petukhova, G.V., Romanienko, P.J., and Camerini-Otero, R.D. (2003). The Hop2 protein has a direct role in promoting interhomolog interactions during mouse meiosis. *Dev. Cell* *5*, 927–936. [https://doi.org/10.1016/s1534-5807\(03\)00369-1](https://doi.org/10.1016/s1534-5807(03)00369-1).
52. Gunn, A., and Stark, J.M. (2012). I-Scel-based assays to examine distinct repair outcomes of mammalian chromosomal double strand breaks. *Methods Mol. Biol.* *920*, 379–391. https://doi.org/10.1007/978-1-61779-998-3_27.
53. Wei, Y., Mizzen, C.A., Cook, R.G., Gorovsky, M.A., and Allis, C.D. (1998). Phosphorylation of histone H3 at serine 10 is correlated with chromosome condensation during mitosis and meiosis in Tetrahymena. *Proc. Natl. Acad. Sci. USA* *95*, 7480–7484. <https://doi.org/10.1073/pnas.95.13.7480>.
54. Schmid, J.A., Berti, M., Walser, F., Raso, M.C., Schmid, F., Krietsch, J., Stoy, H., Zwicky, K., Ursich, S., Freire, R., et al. (2018). Histone ubiquitination by the DNA damage response is required for efficient DNA replication in unperturbed S phase. *Mol. Cell* *71*, 897–910.e8. <https://doi.org/10.1016/j.molcel.2018.07.011>.
55. Lambert, S., and Lopez, B.S. (2001). Role of RAD51 in sister-chromatid exchanges in mammalian cells. *Oncogene* *20*, 6627–6631. <https://doi.org/10.1038/sj.onc.1204813>.
56. Lingg, L., Rottenberg, S., and Francica, P. (2022). Meiotic genes and DNA double strand break repair in cancer. *Front. Genet.* *13*, 831620. <https://doi.org/10.3389/fgene.2022.831620>.
57. Zellweger, R., Dalcher, D., Mutreja, K., Berti, M., Schmid, J.A., Herrador, R., Vindigni, A., and Lopes, M. (2015). Rad51-mediated replication fork reversal is a global response to genotoxic treatments in human cells. *J. Cell Biol.* *208*, 563–579. <https://doi.org/10.1083/jcb.201406099>.
58. Mijic, S., Zellweger, R., Chappidi, N., Berti, M., Jacobs, K., Mutreja, K., Ursich, S., Ray Chaudhuri, A., Nussenzweig, A., Janscak, P., and Lopes, M. (2017). Replication fork reversal triggers fork degradation in BRCA2-defective cells. *Nat. Commun.* *8*, 859. <https://doi.org/10.1038/s41467-017-01164-5>.
59. Schlacher, K., Wu, H., and Jasin, M. (2012). A distinct replication fork protection pathway connects Fanconi anemia tumor suppressors to RAD51-BRCA1/2. *Cancer Cell* *22*, 106–116. <https://doi.org/10.1016/j.ccr.2012.05.015>.
60. Maya-Mendoza, A., Moudry, P., Merchut-Maya, J.M., Lee, M., Strauss, R., and Bartek, J. (2018). High speed of fork progression induces DNA

- replication stress and genomic instability. *Nature* 559, 279–284. <https://doi.org/10.1038/s41586-018-0261-5>.
61. Roy, S., and Schlacher, K. (2019). SIRF: a single-cell assay for in situ protein interaction with nascent DNA replication forks. *Bio Protoc.* 9, e3377. <https://doi.org/10.21769/BioProtoc.3377>.
 62. Qiu, S., Jiang, G., Cao, L., and Huang, J. (2021). Replication fork reversal and protection. *Front. Cell Dev. Biol.* 9, 670392. <https://doi.org/10.3389/fcell.2021.670392>.
 63. Peng, M., Bakker, J.L., Dicioccio, R.A., Gille, J.J.P., Zhao, H., Odunsi, K., Sucheston, L., Jaafar, L., Mivechi, N.F., Waisfisz, Q., and Ko, L. (2013). Inactivating mutations in GT198 in familial and early-onset breast and ovarian cancers. *Genes Cancer* 4, 15–25. <https://doi.org/10.1177/1947601913486344>.
 64. Zhao, W., and Sung, P. (2015). Significance of ligand interactions involving Hop2-Mnd1 and the RAD51 and DMC1 recombinases in homologous DNA repair and XX ovarian dysgenesis. *Nucleic Acids Res.* 43, 4055–4066. <https://doi.org/10.1093/nar/gkv259>.
 65. Huang, F., Motlekar, N.A., Burgwin, C.M., Napper, A.D., Diamond, S.L., and Mazin, A.V. (2011). Identification of specific inhibitors of human RAD51 recombinase using high-throughput screening. *ACS Chem. Biol.* 6, 628–635. <https://doi.org/10.1021/cb100428c>.
 66. Huang, F., Mazina, O.M., Zentner, I.J., Cocklin, S., and Mazin, A.V. (2012). Inhibition of homologous recombination in human cells by targeting RAD51 recombinase. *J. Med. Chem.* 55, 3011–3020. <https://doi.org/10.1021/jm201173g>.
 67. Shkundina, I.S., Gall, A.A., Dick, A., Cocklin, S., and Mazin, A.V. (2021). New RAD51 inhibitors to target homologous recombination in human cells. *Genes* 12, 920. <https://doi.org/10.3390/genes12060920>.
 68. Jaspers, J.E., Kersbergen, A., Boon, U., Sol, W., van Deemter, L., Zander, S.A., Drost, R., Wientjens, E., Ji, J., Aly, A., et al. (2013). Loss of 53BP1 causes PARP inhibitor resistance in Brca1-mutated mouse mammary tumors. *Cancer Discov.* 3, 68–81. <https://doi.org/10.1158/2159-8290.CD-12-0049>.
 69. Evers, B., Drost, R., Schut, E., de Bruin, M., van der Burg, E., Derksen, P.W.B., Holstege, H., Liu, X., van Drunen, E., Beverloo, H.B., et al. (2008). Selective inhibition of BRCA2-deficient mammary tumor cell growth by AZD2281 and cisplatin. *Clin. Cancer Res.* 14, 3916–3925. <https://doi.org/10.1158/1078-0432.CCR-07-4953>.
 70. Henderson, C.J., and Wolf, C.R. (1992). Immunodetection of proteins by Western blotting. *Methods Mol. Biol.* 10, 221–233. <https://doi.org/10.1385/0-89603-204-3:221>.
 71. Blomen, V.A., Májek, P., Jae, L.T., Bigenzahn, J.W., Nieuwenhuis, J., Starling, J., Sacco, R., van Diemen, F.R., Olk, N., Stukalov, A., et al. (2015). Gene essentiality and synthetic lethality in haploid human cells. *Science* 350, 1092–1096. <https://doi.org/10.1126/science.aac7557>.
 72. Li, W., Xu, H., Xiao, T., Cong, L., Love, M.I., Zhang, F., Irizarry, R.A., Liu, J.S., Brown, M., and Liu, X.S. (2014). MAGeCK enables robust identification of essential genes from genome-scale CRISPR/Cas9 knockout screens. *Genome Biol.* 15, 554. <https://doi.org/10.1186/s13059-014-0554-4>.
 73. Nakatani, Y., and Ogryzko, V. (2003). Immunoaffinity purification of mammalian protein complexes. *Methods Enzymol.* 370, 430–444. [https://doi.org/10.1016/S0076-6879\(03\)70037-8](https://doi.org/10.1016/S0076-6879(03)70037-8).
 74. Brinkman, E.K., Chen, T., Amendola, M., and van Steensel, B. (2014). Easy quantitative assessment of genome editing by sequence trace decomposition. *Nucleic Acids Res.* 42, e168. <https://doi.org/10.1093/nar/gku936>.

STAR★METHODS

KEY RESOURCES TABLE

REAGENT or RESOURCE	SOURCE	IDENTIFIER
Antibodies		
Rabbit polyclonal anti-RAD51	Bioacademia	Cat# 70-001; RRID: AB_2177110
Rabbit polyclonal anti-RAD51	Santa Cruz	Cat# sc-8349; RRID: AB_2253533
Rabbit monoclonal anti-RAD51	Abcam	Cat# ab133534; RRID:AB_2722613
Mouse monoclonal CRISPR-Cas9	Novus	Cat# NBP2-36440
Rabbit polyclonal anti-PSMC3IP	Atlas	Cat# HPA044439; RRID:AB_10964210
Rabbit polyclonal anti-PSMC3IP	Proteintech	Cat# 11339-1-AP; RRID:AB_2172642
Rabbit polyclonal anti-MND1	Atlas	Cat# HPA043499; RRID:AB_2732506
Goat polyclonal anti-Rabbit IgG (H+L) Cross-Adsorbed Secondary Antibody, Texas Red-X	Thermo Fisher Scientific	Cat# T-6391; RRID: AB_2556779
Mouse monoclonal Anti-phospho-H2AX (Ser139), clone JBW301	Millipore	Cat# 05-636; RRID:AB_309864
HA-Tag (C29F4) Rabbit mAb	Cell Signaling Technology	Cat# 3724
Mouse monoclonal anti-β-Actin	Sigma	Cat# A2228; RRID: AB_476697
Purified anti-HA.11 Epitope Tag Antibody	BioLegend	Cat# 901501
Rabbit polyclonal anti-biotin	Cell Signaling Technology	Cat# 5597; RRID:AB_10828011
Purified mouse Anti-BrdU/IdU	BD Biosciences	Cat# 347580; RRID:AB_10015219
Rat monoclonal Anti-BrdU/CldU antibody [BU1/75(ICR1)]	Abcam	Cat# ab6326; RRID:AB_305426
Donkey anti-Rat IgG (H+L) Cy3 AffiniPure F(ab') ₂ Fragment	Jackson ImmunoResearch	Cat# 712-165-513; RRID: AB_2340669
Rabbit monoclonal anti-CENPB [EPR24047-64]	Abcam	Cat# ab259855
Rabbit monoclonal anti-phospho RPA32 (S4/S8)	Bethyl Laboratories	Cat# A700-009; RRID:AB_2765278
Rabbit polyclonal anti-53BP1	Abcam	Cat#ab21083; RRID: AB_722496
IgG Fraction Monoclonal Mouse Anti-Biotin	Jackson Immuno research	Cat# 200-002-211; RRID: AB_2339006
Rabbit anti-phospho-HistoneH3-antibody	Cell Signaling Technology	Cat# 9701
Goat anti-Rabbit IgG (H+L) Cross-Adsorbed ReadyProbes™ Secondary Antibody, Alexa Fluor™ 488	Thermo Fisher Scientific	Cat# R37116; RRID: AB_2556544
Goat Anti-Mouse IgG (H+L) Highly Cross-Adsorbed Secondary Antibody, Alexa Fluor 488	Thermo Fisher Scientific	Cat# A-11029; RRID: AB_2534088
Goat polyclonal anti-Rabbit IgG (H+L) Highly Cross-Adsorbed Secondary Antibody, Alexa Fluor 488	Thermo Fisher Scientific	Cat# A-11034; RRID: AB_2576217
Goat Anti-Mouse IgG (H+L) Antibody, Alexa Fluor 555 Conjugated	Thermo Fisher Scientific	Cat # A-21422; RRID:AB_141822
Anti-rabbit IgG, HRP-linked Antibody	Cell Signaling Technology	Cat# 7074; RRID:AB_2099233
Anti-mouse IgG, HRP-linked Antibody	Cell Signaling Technology	Cat# 7076; RRID: AB_330924
IRDye 800CW anti-Rabbit IgG Donkey	LI-COR	Cat# 926-32213; RRID:AB_621848
IRDye 800CW anti-Mouse IgG Goat	LI-COR	Cat # 925-32210; RRID:AB_2687825
IRDye 680RD anti-Mouse IgG Goat	LI-COR	Cat # 926-68070; RRID:AB_10956588

(Continued on next page)

REAGENT or RESOURCE	SOURCE	IDENTIFIER
Continued		
Bacterial and virus strains		
Endura Chemically Competent Cells	Lucigen	Cat# 60240-1
Stellar Competent cells	Takara	Cat# 636763
Chemicals, peptides, and recombinant proteins		
AZD2281 (Olaparib), PARP inhibitor	Syncom, Groningen, the Netherlands	CAS: 763113-22-0
AZD2281 (Olaparib), PARP inhibitor	AstraZeneca	
BMN-673 (Talazoparib), PARP inhibitor	Selleckchem	Cat# S7048; CAS: 1207456-01-6
B02 RAD51 inhibitor	Sigma	Cat# 553525
Nocodazole	Sigma	Cat# M1404
Propidium Iodide	Sigma	Cat# 537060
Hydroxyurea	Sigma Aldrich	Cat# H8627
Mitomycin C	Sigma Aldrich	Cat# M4287
Camptothecin	Sigma Aldrich	Cat# PHL89593
5-Chloro-2'-deoxyuridine (CldU)	Sigma Aldrich	Cat# C6891
5-Iodo-2'-deoxyuridine (IdU)	Sigma Aldrich	Cat# I7125
Colcemid	Sigma Aldrich	Cat# 234109-M
bis-Benzimide	Sigma Aldrich	Cat# H 33258
SSC buffer	Sigma Aldrich	Cat# 85639
Giemsa	Sigma Aldrich	Cat# 32884
Bovine serum albumin	Sigma Aldrich	Cat# A7030
10X RIPA Buffer	Abcam	Cat# ab156034
PhosSTOP Phosphatase Inhibitor Cocktail	Roche	Cat# 4906837001
cOmplete™, Mini Protease Inhibitor Cocktail	Roche	Cat# 11836153001
Critical commercial assays		
QIAamp DNAMini Kit	Qiagen	Cat# 51306
QIAprep Spin Miniprep Kit	Qiagen	Cat# 27106
DNeasy Blood & Tissue Kit	Qiagen	Cat# 69504
HiSpeed Plasmid Maxi Kit	Qiagen	Cat# 12662
MiniElute PCR Purification Kit	Qiagen	Cat# 28006
Click-iT EdU Alexa Fluor 488 Cell Proliferation Kit for Imaging	Thermo Fisher Scientific	Cat# C10337
Duolink proximity Ligation Starter Kit	Sigma	Cat# DUO92101
qPCR Lentivirus Titer Kit	Abm	Cat# LV900
CellTiter-Blue® Cell Viability Assay	Promega	Cat# G8081
CellTiter-Glo® Luminescent Cell Viability Assay	Promega	Ca# G7572
In-Fusion HD Cloning	Takara	Cat# 639650
Phusion Flash High-Fidelity PCR Master Mix	Thermo Fisher Scientific	Cat# F548L
FastStart Universal SYBR Green Master (Rox)	Merck	Cat# 4913850001
TaqMan™ Gene Expression Master Mix	Thermo Fisher Scientific	Cat# 4369016
Dynabeads CD25	Invitrogen	Cat# 11157D
TransIT®-LT1 Transfection Reagent	Mirus	Cat# MIR 2300
Turbfectin 8.0 Transfection Reagent	Origene	Cat# TF81001
Lipofectamine™ 2000 Transfection Reagent	Thermo Fisher Scientific	Cat# 11668019
Lipofectamine™ CRISPRMAX™ Cas9 Transfection Reagent	Thermo Fisher Scientific	Cat# CMAX00003
Lipofectamine™ RNAiMAX Transfection Reagent	Thermo Fisher Scientific	Cat#13778150
Q5 polymerase	New England Biolabs	Cat# M0491S

(Continued on next page)

Continued

REAGENT or RESOURCE	SOURCE	IDENTIFIER
Gateway™ LR Clonase™ II Enzyme mix	Thermo Fisher Scientific	Cat# 11791020
NuPage Novex 4–12% gradient precast gel	Thermo Fisher Scientific	Cat# NP0321BOX
NuPage MOPS SDS Running Buffer	Thermo Fisher Scientific	Cat# NP0001
pCR-TOPO-blunt	Thermo Fisher Scientific	Cat #450245
siGENOME Human MND1 siRNA	Horizon	Cat# D-014779-01 Cat# D-014779-02 Cat# D-014779-03 Cat# D-014779-04 Cat# M-014779-00
siGENOME Human PSMC3IP siRNA	Horizon	Cat# D-018726-01 Cat# D-018726-02 Cat# D-018726-03 Cat# D-018726-04 Cat#:M-018726-01
siGENOME Human PLK1 siRNA	Horizon	Cat# M-003290
siGENOME Human siNTC siRNA	Horizon	Cat# D-001210
siGENOME Human siBRCA1 siRNA	Horizon	Cat# M-003461
siGENOME Human siBRCA2 siRNA	Horizon	Cat# M-003462
RNeasy kit for RNA extraction	Qiagen	Cat # 74004
DNeasy cell and tissue kit	Qiagen	Cat # 69504
High Capacity cDNA Reverse Transcription Kit	Thermo Fisher Scientific	Cat# 4368814
Promega GoScript Reverse Transcription System	Promega	Cat# PRA5000
Edit-R Cas9 nuclease protein NLS	Horizon	Cat# CAS11729
MND1 Taqman probe	Thermo Fisher Scientific	Cat # 4351372 Hs01552130_g1
PSMC3IP Taqman probe	Thermo Fisher Scientific	Cat # 4351372 Hs00917175_g1
GAPDH Taqman probe	Thermo Fisher Scientific	Cat# 4448489 Hs02786624_g1
Formaldehyde solution 4%, buffered, pH 6.9	Sigma Aldrich	Cat# 100496

Deposited data

CRISPR screen data	This paper	Array Express E-MTAB-12929
--------------------	------------	----------------------------

Experimental models: Cell lines

KB1P-G3	PMID: 23103855	N/A
KB1P-G3B1+	PMID: 30530501	N/A
KB2P3.4	PMID: 18559613	N/A
Phoenix ECO	ATCC	RRID:CVCL_H717
HEK293FT	ATCC	RRID:CVCL_6911
KB1P-G3 53BP1 knockout	PMID: 30530501	N/A
HAP1	Gift from Thijn Brummelkamp, NKI, Amsterdam	N/A
HAP1	Horizon	RRID:CVCL_Y019
MCF10A TP53 ^{-/-}	Horizon	Cat# HD+101-005, RRID:CVCL_JM25
MCF10A TP53 ^{-/-} RB1 ^{-/-}	Horizon	N/A
DR-GFP U2OS	Gift from Jeremy Stark, City of Hope, USA,	RRID:CVCL_B0A7
HEK293T	ATCC	RRID:CVCL_0063
SUM149PT	Asterand Bioscience	RRID:CVCL_3422
MDAMB-231	ATCC	RRID:CVCL_0062

Oligonucleotides

sgRNA sequence for KB1P-G3/KB1P-G3B1/KB2P-3.4. non-targeting control: TGATTGGGGTCTTCGCCA	This paper	N/A
Primer sequences used in this study	This paper	See Table S1P

(Continued on next page)

Continued		
REAGENT or RESOURCE	SOURCE	IDENTIFIER
sgRNA sequences used in this study	This paper	See Table S1Q
ORFeome Collab. Hs MND1 ORF w/o Stop Codon	Horizon	Cat# OHS5894-202496657
Recombinant DNA		
pDG459	Addgene	RRID:Addgene_100901
plentiCRISPR v2	Addgene	RRID: Addgene_52961
pOZ_MND1	This paper	N/A
Edit-R Inducible Lentiviral hEF1 α -Blast-Cas9 Nuclease Plasmid DNA	Horizon	Cat# CAS11229
Human genome-wide lentiviral CRISPR gRNA library version 1	Addgene	RRID:Addgene_67989
Plasmid: Lenti-dCas9-KRAB-blast	Addgene	RRID: Addgene_89567
Human genome-wide CRISPRi-V2 library	Addgene	RRID: Addgene_83969
Plasmid: CRISPRi sgRNA backbone	Addgene	RRID: Addgene_50946
Lentiviral packing plasmid psPAX2	Addgene	RRID: Addgene_12260
Lentiviral packing plasmid pMD2.G	Addgene	RRID: Addgene_12259
pRSV-Rev	Addgene	RRID: Addgene_12253
pMDLg/pRRE	Addgene	RRID: Addgene_12251
pCMV-VSV-G	Addgene	RRID: Addgene_8454
pLX302	Addgene	RRID: Addgene_25896
pCBASceI	Addgene	RRID: Addgene_26477
Software and algorithms		
Image J, Fiji, colony area plugin	NIH	https://imagej.nih.gov/ij/download.html
FlowJo	RRID:SCR_008520	Version 10.8.1
GraphPad Prism 9	GraphPad Software	https://www.graphpad.com/
RStudio	RStudio	N/A
SnapGene	SnapGene	N/A
R script to analyse CRISPR screen	This paper	Deposited at Zenodo https://doi.org/10.5281/zenodo.7822892

RESOURCE AVAILABILITY

Lead contact

Further information and requests for resources and reagents should be directed to and will be fulfilled by the lead contact, Christopher Lord (chris.lord@icr.ac.uk).

Materials availability

Further information and requests for resources and reagents should be directed to and will be fulfilled by the [lead contact](#).

Data and code availability

- CRISPR screen data have been deposited at Array Express (E-MTAB-12929) and are publicly available as of the date of publication.
- All original code has been deposited at Zenodo and is publicly available as of the date of publication. DOIs are listed in the [key resources table](#).
- Any additional information required to reanalyze the data reported in this paper is available from the [lead contact](#) upon request.

EXPERIMENTAL MODEL AND SUBJECT DETAILS

Cell lines

MCF10A *TP53*^{-/-} cells were purchased from Horizon (Cat# HD+101-005, RRID:CVCL_JM25). MCF10A *TP53*^{-/-} *RB1*^{-/-} daughter cells generated by CRISPR-Cas9 mutagenesis were purchased from Horizon. MCF10A cells were cultured in Dulbecco's Modified Eagle Medium/Nutrient Mixture F-12 (DMEM/F12, Gibco) supplemented with 5% horse serum; EGF (20 ng/mL); hydrocortisone

(0.5 mg/mL); cholera toxin (100 ng/mL); insulin (10 μ g/mL). DR-GFP U2OS (kindly gifted by Jeremy Stark (City of Hope, USA, RRID:CVCL_B0A7)), HEK293T (ATCC, RRID:CVCL_0063), CAL51 (DSMZ, RRID:CVCL_1110), MDAMB-231 (ATCC, RRID:CVCL_0062) were maintained in Dulbecco's Modified Eagle Medium (DMEM, Gibco) supplemented with 10% fetal bovine serum (FBS, Sigma Aldrich). SUM149 cells (Asterand Bioscience, RRID:CVCL_3422) were maintained in Ham's F-12 medium (Gibco) supplemented with 5% FBS, 10 μ g/mL insulin and 1 μ g/mL hydrocortisone. The KB1P-G3 cell line was previously established from a *K14cre;Brca1^{F/F};Trp53^{F/F}* (KB1P) female mouse mammary tumor.⁶⁸ The KB1P-G3B1 cell line was derived from the KB1P-G3 cell line which was reconstituted with human BRCA1.⁴⁷ The *Tp53bp1* knock out KB1P-G3 line was generated by.⁴⁷ The KB2P-3.4 cell line was previously established from a *K14cre;Brca2^{F/F};Trp53^{F/F}* (KB2P) female mouse mammary tumor.⁶⁹ All these lines were grown in Dulbecco's Modified Eagle Medium/Nutrient Mixture F-12 (DMEM/F12, Gibco) supplemented with 10% fetal calf serum (FCS, Sigma Aldrich), 50 units/mL penicillin-streptomycin (Gibco), 5 μ g/mL Insulin (Cat# I0516, Sigma Aldrich), 5 ng/mL cholera toxin (Sigma Aldrich, Cat# C8052) and 5 ng/mL murine epidermal growth-factor (EGF, Sigma Aldrich, Cat# E4127). The HEK293FT cell line (RRID:CVCL_6911), as well as the Phoenix-ECO cell line (RRID:CVCL_H717), were cultured in Dulbecco's Modified Eagle Medium (DMEM, Gibco) supplemented with 10% fetal calf serum (FCS, Sigma Aldrich) and 50 units/mL penicillin-streptomycin (Gibco). HAP1 cells for PARPI dose/response were purchased from Horizon (RRID:CVCL_Y019) and HAP1 cells for SCE experiments were a kind gift from Thijn Brummelkamp, NKI; these were cultured in IMDM containing 10% FBS, 1% penicillin-streptomycin, and 1 mM L-glutamine (all reagents from Gibco).

Tissue culture was carried out under standard conditions (37°C, 5% CO₂), except for KB1P-G3 and KB2P3.4 cells which were cultured under low oxygen conditions (3% O₂). Testing for mycoplasma contamination was performed on a regular basis.

Reagents

Talazoparib was purchased from Selleckchem and RAD51i B02 was purchased from Sigma (#553525). Olaparib was provided by AstraZeneca. Antibodies utilized for Western blotting are as follows: Anti-MND1 (HPA0434, Atlas), anti-PSMC3IP (HPA044439, Atlas), anti-vinculin (sc-73614, Santa Cruz), anti-HA-tag C29F4 (3724, Cell Signaling), anti-actin (A2228, Sigma), anti-actin anti-V5-tag (Cell Signaling, 13202), anti-Cas9 (NBP2-36440, Novus), anti-actin (C-2) (sc-8432, Santa Cruz).

METHOD DETAILS

Western blotting

Standard protocols for SDS-PAGE and immunoblotting were used.⁷⁰ Whole cell lysate was generated from cell pellets using RIPA Buffer (Abcam) supplemented with PhosSTOP Phosphatase Inhibitor Cocktail (Roche) and cOmplete™, Mini Protease Inhibitor Cocktail (Roche). 50–100 μ g of whole cell lysate was electrophoresed on NuPage Novex 4–12% gradient precast gel (Thermo Fisher Scientific, NP0321BOX) using NuPage MOPS SDS Running Buffer (Thermo Fisher Scientific, NP0001). All gels were run with full range rainbow molecular weight protein marker (NEB, p7712) as a size reference. Proteins were transferred at 100 volts (V) for 1 hour at room temperature (on ice) onto nitrocellulose membranes (GE Healthcare). Membranes were blocked with 5% milk and probed with primary antibody, diluted 1:1,000 in 5% milk overnight at 4°C (details of primary antibodies used are listed in the [key resources table](#)). Secondary antibodies were diluted 1:10,000 in 5% milk and incubated at room temperature for 1 hour (details of secondary antibodies used are listed in the [key resources table](#)). Protein bands were visualised using the Licor Odyssey Fc imaging system.

Haploid genetic screens

See [Figures S1J](#) and [S1K](#). HAP1 cells were mutagenized using a retroviral gene-trap cassette.^{37,71} 1x10⁸ mutagenized HAP1 cells were seeded in 14X T175 cell culture flasks. Cells were irradiated after 24h (day 1), 72h (day 3) and 120h (day 5) with 1.5 Gy each time, which led to a confluency of 70–80% on day 10. Cells were subsequently harvested and fixed and stained for FACS sorting for 1N DNA content. Genomic DNA was isolated from 30 million cells and subjected to Linear Amplification Mediated (LAM)-PCR⁷¹ as follows: 1–2 μ g of DNA was used per 50 μ L reaction (rxn) containing 1 mM MgSO₄, 0.75 pmol doublebiotinylated primer (5'-/double biotin/ggtctccaaatctcggggaac-3'), Accuprime Taq HiFi (0.4 μ L/rxn) and the supplied buffer II (Life technologies). The reaction was performed in 120 cycles with an annealing temperature of 58°C for 30 seconds and an extension temperature of 68°C for 60 seconds. To capture biotinylated single-stranded DNA (ssDNA) products, PCR reactions were combined with M270 streptavidin-coated magnetic beads (Life Technologies) in 2x binding buffer (6 M LiCl, 10 mM Tris, 1 mM EDTA, pH = 7.5) for 2 hours at room temperature and subsequently captured using a magnet. Prior to binding, the beads were washed once in PBS-containing 0.1% bovine serum albumin (BSA) in 1.5 mL non-stick tubes (Life Technologies). Following magnetic precipitation, beads were washed three times with PBS containing 0.05% Triton X-100 (Sigma) prior to linker ligation. A ssDNA linker (5'/phospho/atcgtatgccgtcttctgcttgactcag tagttgtgcgatggattgatg/dideoxycytidine/3') was ligated to the 3' end of biotinylated products in N x 10 μ L reactions containing 2.5 mM MnCl₂, 1 M betaine, 12.5 pmol linker, 1 μ L and 0.5 μ L of Circigase II (Illumina) buffer and enzyme respectively, with N = number of LAM-PCR reactions. All ligation reactions occurred at 60°C for 2 hours in non-stick 1.5 mL tubes (Life Technologies) and were followed by three washes with PBS with 0.05% Triton X-100 (Sigma) after 20 minutes incubation at room temperature. Subsequently, a PCR reaction was performed that introduced the adaptors sequences required for Illumina sequencing (P5 and P7) N x 50 μ L reactions containing 25 pmol of each primer, 5 μ L buffer II and 0.6 μ L Accuprime Taq HiFi (Life technologies) with N = 0.5 X No.

of LAM-PCR reactions). 6 This final amplification was carried out using 18 cycles and an annealing temperature of 55°C for 30s followed by an extension (at 68°C) for 105 s using primers: 5'- aatgatacggcgaccaccgagatctgatggttctctagcttgc-3' and 5'- caagca gaagacggcatacga-3'. Products were purified (PCR purification kit, Qiagen) and sequenced as 51bp or 65bp single-reads (18 picomolar loading concentration) on an Illumina HiSeq2000 (Illumina) or HiSeq2500 (Illumina) using sequencing primer 5'-ctagcttgc aaacctacaggtgggtcttca-3'. Insertion sites were defined by aligning reads to the human genome (GRCh37) and selecting for reads that uniquely align allowing for a single mismatch. Four independent cultured wild-type control datasets were used for normalization.⁷¹ The irradiation screens were performed twice with individual mutagenized HAP1 batches. “Hit” genes were defined as those that passed a FDR-corrected binominal test threshold of $p < 0.05$. To estimate the dose-response of HAP1 wild-type cells to IR, 1,000 cells were seeded in a 24-well plate on day 0. IR treatment at indicated doses was applied after 24h, 72h and 120h, as in the haploid genetic screen. On day 10, cell viability was assessed by adding Cell Titer Blue (Promega) and measuring the absorbance after 4h incubation at 37°C in a Varioskan LUX microplate reader (Thermo Fisher Scientific).

CRISPR screens

Inducible Cas9 MCF10A *TP53*^{-/-} cells were generated for the CRISPRn screen by lentiviral transduction of MCF10A *TP53*^{-/-} cells with hEF1a-Cas9 (Cat# CAS11229, Dharmacon). Following antibiotic selection with 10 µg/mL blasticidin, 300 million Cas9-expressing cells were infected with a genome-wide human lentiviral CRISPR library (RRID:Addgene_67989).³⁰ The cells were infected with a multiplicity of infection (MOI) 0.3 (to ensure <1 sgRNA per cell), resulting in each sgRNA infecting at least 1,000 cells, a representation that was maintained throughout the experiment. The library contains 90,709 sgRNAs targeting 18,010 genes. Following 2 µg/mL puromycin selection for 72 hours, 1 µg/mL doxycycline was added for 72 hours to induce Cas9 expression. The cell line used for CRISPRi screen was generated by lentiviral transduction of MCF10A *TP53*^{-/-} cells with lenti-BLAST-dCas9-KRAB (RRID: Addgene_89567) followed by selection with 10 µg/mL blasticidin. 300 million dCas9-KRAB expressing cells were infected at MOI 0.3 with a genome-wide human lentiviral CRISPRi library (RRID: Addgene_84832).³³ The library contains 104,535 sgRNAs targeting 18,905 protein coding genes. In both CRISPRn and CRISPRi screens, cells were collected for an early time point sample of initial library representation (T_0) following selection. 100 million CRISPR mutagenized cells were exposed to concentrations that caused a 20% reduction in cell survival (Surviving Fraction 80, SF_{80}) of either 2.5 µM olaparib or 25 nM talazoparib. 25 million cells were seeded into 4X 5-layer flasks and the indicated drug, or DMSO, was added after 24 hours. In total, cells were exposed to drug or DMSO for 14 days (10 population doublings), after which the cells were recovered (T_1). In order to identify CRISPR guides responsible for modulating PARPi response, sgRNA enrichment and depletion was estimated in cells that survived exposure to PARPi or DMSO using parallel sequencing. In brief, genomic DNA was extracted from T_0 and T_1 cell samples using the DNeasy blood and tissue kit (Qiagen), according to the manufacturer’s protocol. sgRNA sequences were PCR amplified for sequencing on Illumina sequencing (HiSeq 2500), producing >1,000 short-reads per sgRNA within the library. Analysis of the CRISPR screen is described in the analysis methods section. Short-read DNA sequences were aligned to the known sgRNA sequences present in each pool to compare the relative enrichment or depletion of sgRNAs from T_0 vs. T_1 samples in both DMSO and PARPi exposed samples, as follows, to ultimately calculate a normalized drug effect (DE) Z-score ($normZ^{31}$) for each sgRNA targeting a specific gene. MAGeCK (Model-based Analysis of Genome-wide CRISPR/Cas9 Knockout) software was used to generate sgRNA counts according to the sequences present in the genome-wide CRISPR library.⁷² Using normalized read count data from MAGeCK, quality checks were performed (distribution of read counts, clustering of samples), to confirm the robustness of the data. For downstream analysis of sgRNA read count data, three approaches were used for comparative analysis: (1) MAGeCK (2) Z-score and (3) drug effect Z-score. From MAGeCK workflow, we extracted a ranked list of positively selected hits generated using its robust ranking aggregation algorithm (RRA) approach.⁷² For the Z-score approach of analysis, the low abundant guides with a read count of zero in the T_0 sample were initially identified and filtered out. In order to account for variation in the amounts of DNA sequenced, the read counts were converted to parts per ten million (pptm), and then \log_2 -transformed after adding a pseudo count of 0.5. For each screen, Z-scores were calculated for each individual sgRNA, corrected for viability and drug effects, as follows. The DE* Z-score was elucidated by calculating the difference in abundance of each sgRNA between the drug-treated (Drug (T)) and DMSO-treated samples (DMSO(T)) at a matched timepoint. Viability effects (VE^{**}), the rate of decrease of sgRNA abundance in the population over time in the absence of drug treatment, were taken into account by calculating a Z-score between the T_0 (DMSO (T_0)) and DMSO-treated (DMSO (T_1)) sample. Both DE and VE Z-scores were normalized by median absolute deviation*** (MAD). In order to remove variation in drug effect that can be attributed to VE, a linear model of DE vs VE is plotted, which is used to adjust DE, so is referred to as Corrected DE****. In order to assess the overall effect size of each gene, the corrected DE Z-score was normalized to generate a gene-level drug effect Z-score*****.

$$*Drug\ Effect(DE) = \frac{(Drug(T) - DMSO(T)) - median(Drug(T) - DMSO(T))}{MAD(Drug(T) - DMSO(T))}$$

$$**\ Viability\ Effect\ (VE) = \frac{(DMSO(T_1) - DMSO(T_0)) - median(DMSO(T_1) - DMSO(T_0))}{MAD(DMSO(T_1) - DMSO(T_0))}$$

i.e. $Z = (x - \text{median})/\text{median absolute deviation}$

$$***MAD = \text{median } |x_i - \bar{x}|$$

$$****Corrected DE = \frac{(DE - c)}{(VE \times m)}$$

$$****Gene drug effect Zscore = \frac{(\sum sgRNA Zscores)}{(\sqrt{n \text{ of gRNAs}})}$$

In this case, CRISPR mutagenesis of genes resulting in negative gene-level drug-effect Z-score are determined to enhance PARPi sensitivity. We defined genes as “hits” with a gene-level drug effect Z-score threshold of ≤ -3 , for at least two independent significant ($p = 0.05$) sgRNAs, to capture the top $\sim 2\%$ and identify the most profound effects. Ranks for negative selection were generated by sorting results based on their Z-score in ascending order. A final list of “hits” was consolidated from the three approaches, (1) MAGeCK (2) Z-score and (3) drug effect Z-score, by taking the rank product of their ranks.

When comparing CRISPR screen results from different investigators, we performed quantile normalization in order to account for any technical variation across samples. It is a data transformation technique for making two or more data distributions statistically identical to each other. Quantile normalization was done using the R package, preprocessCore built under R version 4.0.3.

To estimate the dose-response of MCF10A wild-type cells to olaparib and talazoparib, 300 cells were seeded in a 384-well plate on day 0. As indicated, PARPi (olaparib or talazoparib) treatment at indicated doses was applied after 24h. On day 5, cell viability was assessed by adding Cell Titer-Glo (Promega) and measuring the luminescence with a microplate reader (Victor X5, Perkin Elmer) after 30 minutes incubation at RT with agitation.

Gene editing and silencing, plasmids, and cloning

Genome editing

Generation of CRISPR/SpCas9 plasmids targeting KB1P-G3B1, KB1P-G3 and KB2P-3.4 cell lines, were performed using a modified version of the lentiCRISPR v2 backbone (RRID: Addgene_52961) in which a puromycin resistance ORF was cloned under the hPGK promoter. For the HAP1 cell line, pDG459 backbone (RRID: Addgene_100901) carrying two sgRNAs was generated. sgRNA sequences were cloned in both backbones using custom DNA oligos (Microsynth) which were melted at 95°C for 5 mins, annealed at RT for 2 hours and subsequently ligated with quick-ligase (NEB) into BsmBI-digested (Fermantas) lentiCRISPR v2 backbone or BbsI-digested (NEB) pDG459 backbone. All constructs sequences were verified by Sanger sequencing. sgRNA sequences are provided in the [key resources table](#).

MCF10A *MND1* and *PSMC3IP* mutant cell lines were engineered using the Edit-R Gene Engineering System (GE Dharmacon). MCF10A TP53^{-/-} cells were seeded at a density of 1 million cells/well in 6-well plates. After 24 hours, cells were transfected with 40 μM Edit-R Cas9 nuclease protein NLS (DE Dharmacon) mixed with 20 μM 2X crRNA and 10 μM tracrRNA using LipofectamineTM CRISPRMAX transfection reagent (Cat #CMAX00003, Thermo Fisher Scientific), according to manufacturer’s instructions. crRNA utilised are as follows; 5'-GCTGACCTCAAGTCCTAGA-3' and 5'-GTGAGGTTGAACACTTACTT-3' were used to target *PSMC3IP*, 5'-CTTGATGAAGAGCTTTACT-3' and 5'-CGGAAGTCTAATTATTATT-3' for *MND1* targeting, 5'-GATACGTCGGTACCGGACCG-3' for non-targeting control. crRNA sequences are also provided in the [key resources table](#). Four days after transfection, cells were FACS-sorted into 96-well plates at one cell per well in drug-free medium. Targeted genome modifications were analysed by Sanger sequencing of PCR products cloned into pCR-TOPO-blunt (Cat #450245, Thermo Fisher Scientific).

MCF10A *MND1* and *PSMC3IP* CRISPRi cell lines were generated by cloning sgRNAs into the BbsI site of the pKLV5-U6sgRNA5-PGKPuroBFP (RRID: Addgene_50946).³⁰ sgRNA sequences are as follows: sgMND1-1: 5'-GCGGCGAAGCCCACACTA-3'; sgMND1-2: 5'-GGTAGCCTCAGTCCTTACCA-3'; PSMC3IP-1: 5'-GCGGGAAAGGCGATGAGTAA-3'; PSMC3IP-2: 5'-GAAGCTGC GGCGGGAGGTAA-3'. sgRNA sequences are also provided in the [key resources table](#). These constructs were lentivirally transduced into MCF10A TP53^{-/-} dCas9 KRAB cells (these were initially generated by lentiviral transduction of MCF10A TP53^{-/-} cells with lenti-BLAST-dCas9-KRAB (RRID: Addgene_89567) followed by selection with 10 $\mu\text{g}/\text{mL}$ blasticidin). The procedure used for lentiviral transduction is described below.

In order to generate cells expressing a *PSMC3IP* mutant associated with D-loop defect (and XX-GD), a human *PSMC3IP* ORF (Dharmacon) was PCR-amplified using primers designed to result in a deletion of glutamic acid at amino acid positive 201 Fw-GCAAGAAGCAGTTCTTTGAGGTTGGGATAGAGACGGATGAAG Rev- CTCAAAGAAGTCTTCTTGCTCTTG. In-fusion reaction was performed to re-circularize the vector. *PSMC3IP* p.Glu201del or wild-type *PSMC3IP* cDNA was cloned into pLX302 (Addgene #25896) expression vector. These constructs were introduced into MCF10A TP53^{-/-} wild-type, *PSMC3IP* CRISPRi or *PSMC3IP* mutant (clone C3) cell lines.

For the HAP1 cell line used for SCE experiments, pDG459 backbone (Addgene #100901) carrying two sgRNAs was generated. Sequences are as follows for HAP1 cell lines. Non-targeting control: TGATTGGGGTTCGTTCCGCA; sgMnd1-1: GAGAAAAGA GAACTCGCATGA; sgMnd1-2: AAGCTTAGTTGATGATGGTA.

Lentiviral transductions

Lentiviral stocks for generating stable cell lines in murine KB1P-G3/KB1P-G3B1/KB2P-3.4 were generated by transient transfection of HEK293FT cells. On day 0, 8×10^6 HEK293FT cells were seeded in 150 cm cell culture dishes and on the next day transiently transfected with lentiviral packaging plasmids psPAX2 (RRID: Addgene_12260) and pMD2.G (RRID: Addgene_12259) and the plentiCR-SIPRV2 vector containing the respective sgRNA or a non-targeting sgRNA using 2x HBS (280mM NaCl, 100mM HEPES, 1.5 mM Na_2HPO_4 , pH 7.22), 2.5 M CaCl_2 and 0.1x TE buffer (10 mM Tris pH 8.0, 1 mM EDTA pH 8.0, diluted 1:10 with dH_2O). After 30 hours, virus-containing supernatant was concentrated by ultracentrifugation at 20,000 rpm for 2h in a SW40 rotor and the virus was finally resuspended in 100 μL PBS. The virus titer was determined using a qPCR Lentivirus Titration Kit (Applied Biological Materials). For lentiviral transduction, 150,000 target cells from both cell lines were seeded in 6-well plates. 24h later, virus at an MOI of 25 was applied with 8 $\mu\text{g}/\text{mL}$ Polybrene (Merck Millipore). Virus-containing medium was replaced with medium containing puromycin (3.5 $\mu\text{g}/\text{mL}$, Gibco) 24h later. Puromycin selection was performed for three days; subsequently cells were expanded and frozen down at early passage. Lentiviral CRISPR-Cas9 KO were generated in KB1P-G3B1, KB1P-G3 and KB2P-3.4 cell lines. The target sites modifications of the polyclonal cell pools were analyzed by TIDE analysis, which is described below.

Lentiviral stocks for generating stable cell lines in human MCF10A were generated by transient transfection of HEK293T cells. On day 0.3 $\times 10^6$ HEK293T cells were seeded in a 6-well plate and on the next day transiently transfected with lentiviral packaging plasmids psPAX2 (RRID: Addgene_12260) and pMD2.G (RRID: Addgene_12259) and plasmid DNA. For instance, the CRISPRi cell lines in the MCF10A TP53^{-/-} background were generated by generating viral particles expressing pKLV-U6gRNA(BbsI)-PGKpuro2ABFP vector containing the respective sgRNA or a non-targeting sgRNA using Lipofectamine 2000 transfection reagent (11668019, Thermo Fisher Scientific) according to the manufacturer's protocol. After 30 hours, virus-containing supernatant virus containing supernatant was harvested and filtered (0.45 μm). For lentiviral transduction, 150,000 cells were seeded in 6-well plates. 24h later, lentivirus was applied. Virus-containing medium was replaced with medium containing puromycin (2 $\mu\text{g}/\text{mL}$, Gibco) 24h later. Puromycin selection was performed for three days; subsequently cells were expanded and frozen down at early passage.

Transfection

For pDG459 transfection of HAP1 cell line, 150,000 target cells were seeded in 6-well plates. 24h later, 2.5 μg of plasmid with Opti-MEM (31985070, Gibco) and TransIT[®]-LT1 Transfection Reagent (Mirus, Cat# MIR 2300) was added to the cells according to manufacturer's protocol. Plasmid containing media was replaced one day later with puromycin (3.5 $\mu\text{g}/\text{mL}$, Gibco) containing medium. Puromycin selection was performed for three days; subsequently cells were expanded and frozen down at early passage. For clonal selection, cells were trypsinized, spun down (1,200 rpm, 5min) and resuspended in FACS buffer (PBS, 1% FCS) to a concentration of 1×10^6 cells/mL. For FACS sorting 10 ng/mL Hoechst staining was added, single cells were sorted into a 96-well plate using a MoFlo ASTRIOS cell sorter (Beckman Coulter). The target site modification of the monoclonal cell lines was determined by PCR as described below.

For siRNA transfection of DR-GFP U2OS cell line, 1.5×10^5 U2OS cells expressing a synthetic HR reporter substrate (DR-GFP⁵²) were reverse transfected with 20 μM siRNA in Opti-MEM (31985070, Gibco) and Lipofectamine[™] RNAiMAX Transfection Reagent (Cat#13778150), according to the manufacturer's protocol. Details for siRNA reagents used are provided in the [key resources table](#). 24h later, 2.5 μg of pCBAScel (RRID: Addgene_26477) with Opti-MEM and Lipofectamine[™] 2000 Transfection Reagent (Cat# 11668019) were added to the cells according to manufacturer's protocol. Plasmid containing media was replaced one day later for fresh media. After 5 days from initial cell seeding, the cells were fixed in 4% PFA (Sigma Aldrich). GFP fluorescence was measured via FACS analysis.

Retroviral transduction of complementation construct

Mnd1 reconstitution was performed using pOZ-N-FH⁷³ plasmid expressing interleukin-2 receptor α chain (IL2R α /CD25) as selection marker. The *Mnd1* coding sequence was ordered from Eurofins with optimized modifications for *mus musculus*. The coding sequence was cloned into pOZ-N-FH using the in-fusion HD cloning kit (Cat# 12141, Takara) (see [key resources table](#)). Retroviral stocks were generated using the Phoenix-ECO cells. On day 0, 1×10^6 cells were seeded in 10 cm cell culture dishes. Transient transfection of the cells was performed with Turbofectin 8.0 (Origene) according to manufacturer's protocol with a few adjustments. 6 μg of the plasmid DNA was applied to the cells with Turbofectin mixture. On day 2 and 3, virus containing supernatant was harvested and filtered (0.45 μm). Transduction of the target cells was performed on last day of harvest by adding 7 $\mu\text{g}/\text{mL}$ Polybrene (Merck Millipore) to the retroviral supernatant and application on the target cells (9 mL/10 cm cell culture dish). Selection of the target cells was performed using the Dynabeads[®] CD25 (Invitrogen, Cat# 11157D) according to manufacturer's protocol.

The *PSMC3IP* coding sequence was sourced from Eurofins. Yeast p.Glu201del was mapped to human to design the primers for amplification of the linear construct. In order to generate PSMC3IP p.Glu201del, 10 ng PSMC3IP cDNA was amplified with Q5 polymerase (New England Biolabs) using a 3-step protocol: (1) 98°C for 30s, (2) 30 cycles at 98°C for 10s, 60°C for 10s and 72°C for 90s, (3) 72°C for 5min. PCR products were purified using the QIAquick PCR purification kit (Qiagen), according to manufacturer's protocol, and submitted with corresponding forward primer for Sanger sequencing to confirm target modifications. Sequences for primers used are provided in the [key resources table](#). PCR amplification was confirmed via gel electrophoresis. Purified PCR amplified DNA was incubated with DpnI restriction enzyme (NEB, Cat# R0176S). Following in-fusion reaction, using the in-fusion HD

cloning kit (Cat# 12141, Takara), DNA was transformed in Stellar Competent cells (Takara, Cat# 636763). Gateway cloning was used to introduce either PSMC3IP or PSMC3IP p.Glu201del into pLX302 expression vector (RRID: Addgene_25896) using Gateway™ LR Clonase™ II Enzyme mix (Thermo Fisher Scientific, Cat# 11791020), according to the manufacturer's protocol, and then transformed into competent cells. PSMC3IP-pLX302 or PSMC3IP p.Glu201del-pLX302 was introduced into MCF10A TP53^{-/-} cells via lentiviral transduction.

gDNA isolation, amplification, and TIDE analysis

To assess modification rate in polyclonal lentiviral CRISPR/SpCas9 KO cell lines, cells were pelleted and genomic DNA was extracted using the QIAmp DNA mini kit (Qiagen) according to manufacturer's protocol. Target loci were amplified using Phusion High Fidelity Polymerase (Thermo Fisher Scientific) using a 3-step protocol: (1) 98°C for 30s, (2) 30cycles at 98°C for 5s, 63.3°C for 10s and 72°C for 15s, (3) 72°C for 5 mins. Reaction mix consisted of 10 μL of 2x Phusion Mastermix (Thermo Fisher Scientific), 1 μL of 20 μM forward and reverse primer and 100 ng of DNA in 20 μL total volume. PCR products were purified using the QIAquick PCR purification kit (Qiagen) according to manufacturer's protocol and submitted with corresponding forward primers for Sanger sequencing to confirm target modifications using the TIDE algorithm.⁷⁴ The target site modification of the monoclonal HAP1 cell lines was determined using two different primer pairs. DNA extraction was performed with QIAmp DNA mini kit (Qiagen). Amplification of target sites with Phusion High Fidelity Polymerase (Thermo Fisher Scientific) was done according to the following 3-step protocol: (1) 98°C for 10s, (2) 30 cycles at 98°C for 1s, 60°C for 5s and 72°C for 15s, (3) 72°C for 1min. One primer pair targets the DNA sequence between the two sgRNAs, therefore a PCR result is only detected in cell lines without mutation of MND1. The other primer pair targets before the first sgRNA and after the second sgRNA, so that a PCR result is only visible if there is a large deletion in MND1 gene.

In vitro cell survival assays

KB1P cells

2,000 KB1P-G3B1 or 4,000 KB1P-G3 cells were seeded per well of a 6-well plate and IR-treated cells were subsequently exposed to repeated irradiation on day 2 and 3. Olaparib treated cells were constantly exposed to olaparib during the course of the experiments. Control wells of the 6-well plates were fixed with 4% formalin and stained with 0.1% crystal violet on day 8, whereas treated cells in 6-well plates were fixed and stained on day 11. Quantification of plates was performed in FIJI image processing package of ImageJ (1.8.0) in an automated manner with macros.

1,000 HAP1 cells were seeded in a 24-well plate and exposed to the indicated drug or irradiation at the indicated dosages after 24 hours. IR-treated cells were subsequently exposed to repeated irradiation on day 2 and 3. Cell viability of HAP1 cell lines in 24-well plates was assessed by adding 25 μL of CellTiter-Blue® Cell Viability Assay (Cat# G8081, Promega) to each well. After 4h incubation at 37°C, absorbance was measured in a Varioskan LUX microplate reader (Thermo Fisher Scientific).

MCF10A cells

MCF10A cells were seeded into 384-well plates at a concentration of 300 cells per well in 50 μL growth medium. After 24 hours, drug or vehicle (DMSO) dilutions in growth media were added to the cells using an Echo liquid handler (Beckman). In 384-well format, cells were continuously exposed to drug for a total of 5 days. MCF10A or HAP1 cells were also plated in 96-well plates at a density of 1,500 cells/well in 100 μL medium and exposed to the indicated drug at the indicated dosages after 24 hours. If RAD51 inhibitor B02 was used, 25 μM B02 (Sigma, 553525) was applied to cells 1 hour before drug- or DMSO treatment. In 96-well format, cells were continuously exposed to drug for a total of ten days. Cell viability was assessed using CellTiter-Glo (CTG) Luminescent Cell Viability Assay (Cat# G7572, Promega). Media was removed from the plate before addition of CTG (diluted 1:4 with 1X PBS) to each well. Plates were continuously shaken and incubated in the dark for 10 minutes at room temperature before measuring luminescence with a microplate reader (Victor X5, Perkin Elmer).

Clonogenic assays

MCF10A or HAP1 cells were seeded into 6-well plates at a density of 500 cells per well in 2 mL growth medium. After 24 hours, media was replaced with drug or vehicle (DMSO) dilutions in growth medium at the indicated concentrations. Drug was replenished every three days for up to 14 days, at which point colonies were fixed with 10% trichloroacetic acid (TCA) for 1 hour at 4°C and stained with sulforhodamine B (SRB, 0.057% sulforhodamine B (w/v) in 1% acetic acid) for 1 hour at room temperature. Excess dye was removed by washing plates with 1% acetic acid. KB1P-G3B1 cells were seeded in 10 cm² dishes at a density of 100 cells/dish. Cells were exposed to PARPi 24 h later. Following 15 days of PARPi selection, colonies were fixed with 4% formalin and stained with 0.1% crystal violet. All colonies were counted in an automated manner using the colony counter tool with ImageJ.

For Figures 1B, 1C, 2B, 2D, 2G, 2H, 4B, 4H, 4I, S1H, S1M, S1N, S5A–S5D, S5J, S5K, and S13B: all experiments indicated in these figures were performed as at least three replicates and graphs were drawn from these data using GraphPad Prism 9. Surviving fraction was calculated for each drug dose relative to DMSO-exposed cells. In the case of S4G and S4H, surviving fraction was calculated for each IR dose relative to untreated control. Error bars represent standard deviation (SD). Data was fitted to four parameter logistic (4PL) sigmoidal curve and the *P*-values were calculated via 2-way ANOVA with Tukey's post-test.

For Figures 2A, 2C, 2M, S5H, and S5I: all experiments indicated in these figures were performed as at least two replicates and graphs were drawn from these data using GraphPad Prism 9. Surviving fraction was calculated for each drug dose relative to DMSO-exposed cells. Error bars represent SD. Data was fitted to four parameter logistic (4PL) sigmoidal curve and the *P*-values were calculated via 2-way ANOVA with Tukey's post-test.

For [Figures 2I, 2N, S5E, and S5L](#): all experiments indicated in these figures were performed as at least two individual biological replicates and graphs were drawn from these data using GraphPad Prism 9. Each condition was normalized to the corresponding untreated control. Data was fitted to four parameter logistic (4PL) sigmoidal curve and the *P*-values were calculated via 2-way ANOVA with Tukey's post-test. Error bars represent SD.

RAD51 and γ H2AX immunofluorescence assays

See [Figures 3C–3E, 4C–4F, S6E, S7A, S7D, S8D, S12E, S12F, and S13D](#). In the case of [Figures S6E, S8D, S13D, 3C, 3E, and 4C–4F](#). CRISPR/SpCas9-modified KB1P-G3 and KB1P-G3B1 cells were grown on coverslips in 24-well plates. Irradiation induced foci (IRIF) were induced by γ -irradiation (10 Gy) 3 hours prior to fixation or at the indicated time points. 25 nM talazoparib was also used to induce RAD51 and γ H2AX foci, 72 hours prior to fixation. Subsequently, cells were washed in PBS and fixed with 4% PFA/PBS for 20 mins on ice. Fixed cells were washed with PBS and were permeabilized for 20 mins in 0.2% Triton X-100/PBS. All subsequent steps were performed in staining buffer (PBS, BSA (2%), glycine (0.15%), Triton X-100 (0.1%)). Cells were washed 3 times and blocked for 30 mins at RT, followed by incubation with the primary antibody for 1 hour at RT with rabbit-anti-RAD51 (AB_2177110, Cat# 70-001, BioAcademia) or mouse-anti-phospho-H2AX (RRID: AB_309864, Millipore) or rabbit anti-HA-Tag (#3724, Cell Signaling). Coverslips were then washed 3 times, incubated with the secondary antibody for 1 hour at RT with Goat anti-Rabbit IgG (H+L) Cross-Adsorbed Secondary Antibody, Texas Red-X (RRID: AB_2556779, Cat# T-6391, Thermo Fisher Scientific) or Goat anti-mouse IgG (H+L) Highly Cross-Adsorbed secondary antibody, Alexa Fluor 488 (RRID: AB_2534088, Thermo Fisher Scientific), washed 3 times, counterstained with DAPI (Life Technologies, 1:50,000 dilution) and washed 5 times more before mounting. Antibodies were diluted in staining buffer. Lastly, cells were mounted using fluorescence mounting medium (S3023, Dako). Fluorescent images were acquired using a Delta Vision widefield microscope (GE Healthcare Life Sciences) and multiple different fields were imaged per sample (60 \times objective).

For MCF10A TP53^{-/-} cells, 75,000 cells were plated onto coverslips pre-coated with 50 μ g/mL poly-L-lysine (P2636, Sigma Aldrich) in 24-well plates. The following day, cells were fixed either 16 hours post 10 μ M olaparib or 0.1 μ M talazoparib treatment, or 3 hours post IR (10 Gy) exposure. Control cells were either exposed to DMSO or no IR. If RAD51 inhibitor B02 was used, 25 μ M B02 (Sigma, 553525) was applied to cells 1 hour before drug- or DMSO treatment. Prior to fixation, cells were permeabilized for 5 mins at RT in permeabilization buffer (20 mM TRIS-HCl, 50 mM NaCl, 3 mM MgCl₂, 1 M sucrose, 0.5% Triton X-100) following a PBS wash step. Cells were fixed in 4% PFA (Sigma Aldrich) for 20 mins at RT. Fixed cells were washed with PBS and were permeabilized for 20 mins in permeabilization buffer (20 mM TRIS-HCl, 50 mM NaCl, 3 mM MgCl₂, 1 M sucrose, 0.5% Triton X-100). Cells were washed 3 times in PBS and blocked in IFF (5% BSA (bovine serum albumin) in PBS with 0.2% Tween) for 30 minutes at RT, incubated with the primary antibodies overnight at 4 $^{\circ}$ C; rabbit anti-RAD51 (RRID:AB_2253533, Cat# sc-8349 (H-92), Santa Cruz) 1:2,000 dilution, and mouse-anti-phospho-H2AX (RRID: AB_309864, Millipore) 1:2,000 dilution. Coverslips were washed 3 times, then incubated with the secondary antibodies for 1 hour at RT; Goat Anti-Mouse IgG (H+L) Antibody, Alexa Fluor 555 Conjugated (Cat# A-21422, RRID:AB_141822, Thermo Fisher Scientific), Thermo Fisher Scientific) and Goat polyclonal anti-Rabbit IgG (H+L) Highly Cross-Adsorbed Secondary Antibody, Alexa Fluor 488 (Cat# A-11034, RRID: AB_2576217, Thermo Fisher Scientific) at 1:1,000 dilution. Coverslips were washed 3 times in PBS before mounting onto glass slides using ProLongTM Diamond Antifade Mountant with DAPI (Cat #P36962, Thermo Fisher Scientific). Z-stack images were acquired using the Marianas advanced spinning disk confocal microscope (3i) and multiple different fields were imaged per sample (63 \times objective).

For all foci experiments, images were analyzed and foci quantification analysis was performed using FIJI image processing package of ImageJ (1.8.0). All nuclei were detected by the “analyze particles” command and all the foci per nucleus were counted with the “finding maxima” command. Foci quantification data was graphed using GraphPad Prism 9. *P*-values were calculated via one-way ANOVA with Bonferroni post-test in the case of [Figures 3C–3E, 4C–4F, S6E, S7A, S7D, S8D, S12E, and S12F](#). In the case of [Figure 3D](#), *P*-values were calculated via one-way ANOVA with Sidak's post-test. Error bars represent the median and 95% CI.

Single-molecule DNA fiber assay

See [Figures 3I–3K](#). Asynchronously growing subconfluent KB1P-G3B1 or KB1P-G3 cells were labeled with 30 μ M thymidine analogue 5-chloro-2'-deoxyuridine (CldU) (Cat# C6891, Sigma Aldrich) for 20 mins, washed three times with warm PBS and subsequently exposed to 250 μ M of 5-iodo-2'-deoxyuridine (IdU) for 20 mins. In the experiment assessing replication fork stability, IdU pulse was followed by adding medium containing 8 mM hydroxyurea (HU) for 6 h for KB1P-G3B1 cells or 4 mM HU for 3h for KB1P-G3 cells. To assess replication fork reversal KB1P-G3 cells were treated with 600 nM Mitomycin C (MMC) ahead of pulse labeling with CldU and IdU as described before, MMC treatment was maintained during labeling. All cells were then collected by standard trypsinization and resuspended in cold PBS at 3.5 \times 10⁵ cells/mL. The labeled cells were mixed 1:5 with unlabeled cells resuspended in cold PBS in the concentration 2.5 \times 10⁵ cells/mL. 2.5 μ L of this cell suspension was then mixed with 7.5 μ L of lysis buffer (200 mM Tris-HCl, pH 7.4, 50 mM EDTA, and 0.5% (v/v) SDS) on a positively-charged microscope slide. After 9 mins of incubation at RT, the slides were tilted at an approximately 30–45 $^{\circ}$ angle to stretch the DNA fibers onto the slide. The resulting DNA spreads were air-dried, fixed in 3:1 methanol/acetic acid, and stored at 4 $^{\circ}$ C overnight. Next day, the DNA fibers were denatured by incubation in 2.5 M HCl for 1 h at RT, washed five times with PBS and blocked with 2% (w/v) BSA in 0.1% (v/v) PBST (PBS and Tween 20) for 40 mins at RT while gently shaking. The newly replicated CldU and IdU tracks were stained for 2.5 h at RT using two different anti-BrdU antibodies recognizing CldU (RRID:AB_305426, Cat# ab6326, Abcam) and IdU (RRID:AB_10015219, Cat#

347580, Becton Dickinson), respectively. After washing five times with PBS-T (PBS and Tween 20) the slides were stained with goat anti-mouse IgG (H+L) Cross-Adsorbed Secondary Antibody, Alexa Fluor 488 (RRID: AB_2534088, Cat# A-11029, Thermo Fisher Scientific) diluted 1:300 in blocking buffer and with the Cy3 AffiniPure F(ab')₂ Fragment Donkey Anti-Rat IgG (H+L) antibody (Cat# 712-165-513, Jackson ImmunoResearch) diluted 1:150 in blocking buffer. Incubation with secondary antibodies was carried out for 1 h at RT in the dark. The slides were washed five times for 3 mins in PBS-T, air-dried and mounted in Fluorescence mounting medium (Cat# S3023, Dako). Fluorescent images were acquired using the DeltaVision Elite widefield microscope (GE Healthcare Life Sciences). Multiple fields of view from at least two slides (technical replicates) of each sample were imaged using the Olympus 60X/1.42, Plan Apo N, UIS2, 1-U2B933 objective and sCMOS camera at the resolution 2048 × 2048 pixels. To assess fork progression CldU + IdU track lengths of at least 120 fibers per sample were measured using the line tool with FIJI image processing package of ImageJ (1.8.0). Replication fork stability was analyzed by measuring the track lengths of CldU and IdU separately and by calculating IdU/CldU ratio. Track lengths were plotted in GraphPad Prism 9 and *P*-values were calculated via 2-way ANOVA with Tukey's post-test. Error bars represent the median and 95% CI.

Analysis of micronuclei formation

See Figures 3L, 3M, and S11K–S11Q. Cells were seeded on coverslips in 24-well plates and treated with DMSO or indicated concentrations of olaparib or irradiated with the indicated dosages 24h later. After 48h of treatment, cells were washed with PBS and fixed with 4% (v/v) PFA/PBS for 20 mins in RT. Cells were then washed 3 times in 0.2% (v/v) PBS-Tween-20 and permeabilized for 20 mins in 0.2% (v/v) Triton X-100/PBS. Then, slides were washed 3 times with PBS and blocked for 30 mins at RT in staining buffer (PBS, BSA (2%), glycine (0.15%), Triton X-100 (0.1%)). For micronuclei staining only, slides were counterstained with DAPI (1:50,000 dilution, Cat# D1306, Life Technologies) and washed 5 times more with PBS before mounting in Fluorescence mounting medium (Cat# S3023, Dako). For co-staining with CENPB, slides were blocked for 30 mins at RT and incubated with primary antibody rabbit-anti-CENPB (Cat# ab259855, abcam) for 1 h at RT, washed 3 times, incubated with the secondary antibody for 1 hour at RT with Goat anti-mouse IgG (H+L) Highly Cross-Adsorbed secondary antibody, Alexa Fluor 488 (RRID: AB_2534088, Thermo Fisher Scientific), washed 3 times, counterstained with DAPI (Life Technologies, 1:5,000 dilution) and washed 5 times more with PBS before mounting in Fluorescence mounting medium (Cat# S3023, Dako). Z-stack images were acquired using the DeltaVision Elite widefield microscope (GE Healthcare Life Sciences). Multiple fields of view were imaged per sample with Olympus 100X/1.40, UPLS Apo, UIS2, 1-U2B836 objective and sCMOS camera. Frequency of micronuclei positive cells was analyzed manually in FIJI image processing package of ImageJ (1.8.0). Scatterplot graphs of % cells with micronuclei (*n* = 20) in each indicated sample were drawn using GraphPad Prism 9. Error bars represent the median and 95% (confidence interval) CI. *P*-values were calculated via 2-way ANOVA with Tukey's post-test.

Flow cytometric analysis

See Figures 3G and S10D–S10G. KB1P-G3B1 cells in a 10 cm cell culture dish were treated with 10 μM camptothecin or left untreated. After 5h incubation, cells were harvested and washed 1x with PBS. Cells were subsequently fixed with 1 mL 4% PFA for 10 mins at 37°C, washed with PBS and permeabilized with 1 mL 0.2% Triton-X-100 for 30 mins on ice. Subsequently, cells were washed with FACS buffer (PBS, 10% FCS (Gibco)), and incubated with rabbit-anti-phospho-RPA32 (Cat# A300-245A, Bethyl Laboratories) for 1 h at RT, washed 2x with FACS buffer and incubated with Goat anti-rabbit IgG (H+L) Highly Cross-Adsorbed secondary antibody, Alexa Fluor 488 (RRID: AB_2576217, Thermo Fisher Scientific) and 1 mg/mL DAPI (Cat# D1306, Life technologies) for 1 h at RT, washed twice with FACS buffer and resuspended in 1 mL FACS buffer. Flow cytometry was performed with BD LSR II Flow Cytometer (BD Biosciences). At least 10,000 events per biological replica and at least two biological replicas were analyzed for each experiment. Data were processed using FlowJo software. In the case of Figure 3G, *P*-values were calculated via one-way ANOVA followed by Dunnet's multiple comparison test. In the case of Figure S10E, *P*-values were calculated via unpaired t-test.

Proximity ligation assay (PLA)

See Figures 3A, 3B, and 3H. KB1P-G3B1 cells were seeded on sterile glass coverslips in a 24-well plate 48 h before the experiment. Cells were treated with 10 Gy irradiation and after 3 h incubation, washed three times with PBS, pre-extracted for 5 min with CSK buffer (25 mM HEPES, pH 7.5, 50 mM NaCl, 1 mM EDTA, 3 mM MgCl₂, 300 mM sucrose and 0.5% (v/v) Triton X-100) on ice and fixed with 4% (v/v) PFA/PBS for 20 mins on ice. Next, slides were permeabilized with 0.2% (v/v) Triton X-100 for 20 mins at RT and blocked with staining buffer (PBS, BSA (2% w/v), glycine (0.15% w/v), Triton X-100 (0.1% v/v)) for 1 h at RT. Incubation with the indicated primary antibodies rabbit-anti-RAD51 (Cat# 70-001, Bioacademia), mouse-anti-phospho-H2AX (RRID: AB_309864, Millipore) and rabbit-anti-HA-Tag (Cat# 3724, Cell Signaling) or mouse-anti-HA-Tag (#901501, BioLegend) in staining buffer was carried out at 4°C overnight. The next day, the slides were washed two times with staining buffer and *in situ* proximity ligation was performed according to the Duolink Detection Kit protocol (Cat# DUO92101, Sigma Aldrich). Z-stack images were acquired using the DeltaVision Elite widefield microscope (GE Healthcare Life Sciences). Multiple fields of view were imaged per sample with Olympus 100X/1.40, UPLS Apo, UIS2, 1-U2B836 objective and sCMOS camera. Each image was taken in 5 Z-layers and Z axis is projected into one layer for quantification. Images were analyzed using the FIJI image processing package of ImageJ (1.8.0); each nucleus was defined as a particle by thresholding (analyze particles command) and PLA foci per cell were quantified

with the “find maxima” command in each defined particle. At least 100 cells were quantified from each condition and graphed using GraphPad Prism 9. *P*-values were calculated via 2-way ANOVA with Tukey’s post-test.

In situ analysis of protein interactions at DNA replication forks (SIRF)

KB1P-G3B1 cells were seeded on sterile glass coverslips in a 24-well plate 48h before the experiment in the density of 30,000 cells/well. EdU labeling was performed by adding 25 μ M EdU in the medium for 10 mins. After three washes with PBS, replication stress was induced in the HU-treated samples by adding 2 mM HU for 2h. Cells were then washed twice with PBS and nuclei were pre-extracted with CSK buffer (10 mM PIPES pH 7, 0.1 M NaCl, 0.3 M sucrose, 3 mM MgCl₂, 0.5% (v/v) Triton X-100) on ice for 5 mins. After pre-extraction, cells were washed with PBS and fixed in 4% (v/v) PFA/PBS for 20 mins on ice. After three washes with PBS, permeabilization was performed with 0.2% (v/v) Triton X-100 for 20 mins at RT. Then, click reaction was performed by adding the click reaction buffer (100 mM Tris pH 8, 4 mM CuSO₄, 100 mM sodium ascorbate, 50 μ M biotin-azide) to the samples and incubating at 37°C for 2h. Slides were then incubated in the blocking buffer (PBS, BSA (2% w/v), glycine (0.15% w/v), Triton X-100 (0.1% v/v)) for 1 h at 37°C, followed by incubation with primary antibodies mouse-anti-HA-Tag (Cat# 901501, BioLegend) and rabbit-anti-biotin (Cat# 5597, Cell Signaling) overnight at 4°C. The next steps are identical to the steps described in the PLA protocol above.

Sister chromatid exchange assay

See [Figures S10B](#) and [S10C](#). HAP1 cells were treated for 48 hours treatment with 10 μ M BrdU. If indicated, 0.5 μ M olaparib (Axon Medchem) was added simultaneously with BrdU. Colcemid was added for the last 3 hours at a concentration of 100 ng/mL. Alternatively, cells were treated with 3 Gy γ -irradiation 8–10 h prior to fixation using an IBL 637 Cesium137 γ -ray machine. Cells were and inflated in a hypotonic 0.075 M KCl solution, and subsequently fixed in 3:1 methanol:acetic acid solution. Metaphase spreads were made by dripping the cell suspensions onto microscope glasses from a height of \sim 30 cm. Slides were stained with 10 μ g/mL bis-Benzimide H 33258 (Sigma Aldrich) for 30 minutes, exposed to 245 nM UV light for 30 minutes, incubated in 2x SSC buffer (Sigma Aldrich) at 60°C for 1 h, and stained in 5% Giemsa (Sigma Aldrich) for 15 minutes. All experiments indicated in these figures were performed in three replicates and graphs were drawn from these data using GraphPad Prism 9. *P*-values were calculated via one-way ANOVA followed by Sidak’s multiple comparison test. Error bars represent the median and 95% CI.

G2-arrest analysis

HAP1 cells were either left untreated, treated for 16 hours with nocodazole (250 ng/ml), or treated with 2.5 Gy IR (Cesium137 source, CIS Bio international/IBL637 irradiator) at 30 minutes prior to 16h nocodazole treatment. Cells were fixed in icecold 70% ethanol and stained with propidium iodide (50 μ g/ml)/RNase (100 μ g/ml) and rabbit-anti-phospho-HistoneH3-antibody (Cat# 9701, Cell Signaling) and goat-anti-rabbit-Alexa-488-conjugated secondary antibody (Cat# R37116, Thermo Fisher Scientific). At least 10,000 events were analyzed per sample on a Quanteon (Agilent).

qRT-PCR

See [Figures S3A](#), [S3B](#), [S4I](#), [S4J](#), [S5G](#), [S9A](#), and [S9B](#). Total RNA was isolated (Qiagen RNAeasy) and 1,000 ng RNA was reverse transcribed with High Capacity cDNA Reverse Transcription Kit (Cat# 4368814, Thermo Fisher Scientific), or with the Promega GoScript Reverse Transcription System (#PRA5000, Promega), as per kit instructions. 25 ng cDNA was amplified with 125 nM Hs01552130_g1 MND1 TaqMan probe human (Cat# 4351372, Thermo Fisher Scientific) or Hs00917175_g1 PSMC3IP TaqMan probe human (Cat# 4351372, Thermo Fisher Scientific) and Hs02786624_g1 GAPDH TaqMan probe human (4448489, Thermo Fisher Scientific) with TaqMan master mix. The mouse *Mnd1* cDNAs were amplified with the FastStart Universal SYBR Green Master (Rox) (4913850001, Merck), using different primers for the endogenous and rescue MND1 cDNA where the sequence was optimized for re-expression in murine cells. Primer sequences are indicated in the [key resources table](#). QuantStudio 6 Flex Real-Time PCR System (Thermo Fisher Scientific) was used for quantification. Fold depletion for CRISPR mutagenized cells or each siRNA treatment was determined as $2^{\Delta\Delta Ct}$, for which the cycle threshold (Ct) value for the target mRNA was subtracted by Ct value for GAPDH (mean of duplicate amplifications from the same RT reaction) to calculate the ΔCt value, which was then subtracted from the corresponding ΔCt from wild-type or siCTRL treated cells to calculate $\Delta\Delta Ct$. Data was plotted in GraphPad Prism 9. Error bars represent SD from *n* = 3 replicates. *P*-values were calculated via one-way ANOVA followed by Dunnett’s multiple comparison test in the case of [Figures S3A](#), [S3B](#), [S4I](#), and [S4J](#). In the case of [Figures S9A](#) and [S9B](#), *P*-values were calculated via one-way ANOVA followed by Sidak’s multiple comparison test. In the case of [S5G](#), *P*-values were calculated via unpaired t-test.

QUANTIFICATION AND STATISTICAL ANALYSIS

Statistical tests were carried out using GraphPad Prism 9. Details describing each statistical test are described in [STAR Methods](#) and summary statistics are provided, where appropriate, on each figure.